

New Ionization Models and the Shocking Nitrogen Excess at $z > 5$

Sophia R. Flury^{1,2*}, Karla Z. Arellano-Córdova¹, Edward C. Moran,³ and Alaina Einsig^{2,3}

¹*Institute for Astronomy, University of Edinburgh, Royal Observatory, Edinburgh, EH9 3HJ, UK*

²*Department of Astronomy, University of Massachusetts Amherst, Amherst, MA 01002, USA*

³*Department of Astronomy, Van Vleck Observatory, Wesleyan University, 96 Foss Hill Drive, Middletown, CT 06459, USA*

Accepted XXX. Received YYY; in original form ZZZ

ABSTRACT

The new era of galaxy evolution studies hearkened in by *JWST* has led to the discovery of $z > 5$ galaxies exhibiting excess nitrogen with $\log(\text{N}/\text{O}) \sim 1$ dex or more than expected from $\log(\text{N}/\text{O}) - 12 + \log(\text{O}/\text{H})$ trends in the local Universe. A variety of novel enrichment pathways have been presented to explain the apparent nitrogen excess, invoking a wide range of processes from very massive stars to stripped binaries to fine-tuned star-formation histories. However, understanding the excitation mechanism responsible for the observed nebular emission is necessary to accurately infer chemical abundances. As of yet, the ionization sources of these galaxies have not been thoroughly explored, with radiative shocks left out of the picture. We present a suite of homogeneous excitation models for star-forming galaxies, active galactic nuclei, and radiative shocks, with which we explore possible explanations for the apparent nitrogen excess. We propose new BPT-style diagnostics to classify galaxies at $z > 5$, finding that, when combined with $\text{O III}] \lambda\lambda 1660,66$ and $\text{He II} \lambda 1640$, $\text{N III}] \lambda\lambda 1747-54 / \text{C III}] \lambda\lambda 1907,09$ best selects shock-dominated galaxies while $\text{N IV}] \lambda\lambda 1483,86 / \text{C III}] \lambda\lambda 1907,09$ best distinguishes between active black holes and star forming galaxies. From our diagnostics, we find that slow/intermediate radiative shocks ($v = 75\text{--}150 \text{ km s}^{-1}$) are most consistent with observed UV emission line flux ratios in nitrogen-bright galaxies. Accounting for the effects of shocks can bring nitrogen estimates into better agreement with abundance patterns observed in the local Universe and may be attributable to Wolf Rayet populations actively enriching these galaxies with nitrogen and possibly driving winds responsible for these shocks.

Key words: galaxies: ISM – galaxies: abundances – ISM: abundances – ultraviolet: galaxies

1 INTRODUCTION

With the dawn of the *JWST* era, reports of enhanced nitrogen in multiple galaxies at high redshift ($z > 5$) have astounded the astronomical community. Notable cases include GHZ2 ($z = 12.4$, Castellano et al. 2024), GN-z11 ($z = 10.6$, Bunker et al. 2023; Senchyna et al. 2023), CEERS-1019 ($z = 8.678$, Larson et al. 2023; Marques-Chaves et al. 2024), and GS 3073 ($z = 5.55$, Ji et al. 2024). Standard chemical evolution models based on nucleosynthesis and stellar yields struggle to explain high $\log(\text{N}/\text{O})$ ratios in general (e.g., Kobayashi et al. 2020). Explanations of the nitrogen excess at $z > 5$ invoke multi-burst star formation scenarios with particularly narrow time windows (< 1 Myr) during which such high $\log(\text{N}/\text{O})$ is attainable (Kobayashi & Ferrara 2024), low-metallicity stripped binary stars in proto globular clusters (Senchyna et al. 2023; Isobe et al. 2023), very massive stars (VMS, e.g., Vink 2023; Emil Rivera-Thorsen et al. 2024; Nandal et al. 2024a), or rapidly rotating Population III stars with fine-tuned abundance yields (Nandal et al. 2024b). Moreover, the gas excitation mechanism remains wholly ambiguous. Both GN-z11 and GHZ2 reside ambiguously on the threshold between active galactic nuclei (AGN) and starburst photoionization model predictions (Bunker et al. 2023; Castellano et al. 2024) with additional evidence suggestive of an AGN (Maiolino et al. 2024). CEERS-1019 exhibits evidence for

both VMS (Marques-Chaves et al. 2024) and a supermassive black hole (SMBH, Larson et al. 2023; Marques-Chaves et al. 2024).

Clearly, follow-up investigation is necessary to understand the origins of both the nitrogen enhancement and the gas excitation in these esoteric yet fundamentally important galaxies. Among the excitation mechanisms considered in the literature regarding galaxies with reported nitrogen excess, one remains strangely absent: shocks. A variety of phenomena can cause radiative shocks, including supernovae, stellar winds, and outflows (e.g., Draine & McKee 1993; Sutherland et al. 1993; Dopita 1995; Allen et al. 2008), all of which occur in galaxies across cosmic time and are thus reasonable to consider as an alternative to those proposed in the literature. However, comparing existing published shock and photoionization model libraries comes with several caveats which complicate their simultaneous use to characterize ionization mechanisms, including differences in abundance patterns (e.g., Nicholls et al. 2017) and in atomic data and underlying physics (e.g., Zhu et al. 2023).

The popular photoionization code Cloudy (Ferland et al. 2017) does not support shock models. As a result, the current libraries of photoionization models in active use, built using Cloudy—noteably Gutkin et al. (2016) for star-forming galaxies (SFGs) and Feltre et al. (2016) for AGN—utilize a different implementation of atomic data and radiative transfer and ionization equilibrium solutions than the most contemporary Alarie & Morisset (2019) shock model library EOMS, built using MAPPINGS V (Sutherland & Dopita 2017; Sutherland et al. 2018). The variations between the Cloudy and MAPPINGS V codes

* E-mail: sflury@roe.ac.uk

can lead to systematic differences of anywhere from 25 to 300% in predicted line fluxes (e.g., [Zhu et al. 2023](#)). None of these libraries use empirical abundance patterns based on O and B stars and are therefore more likely biased by systematics associated with, e.g., scaling with solar abundances or fits to H II region measurements (e.g., [Gutkin et al. 2016](#)). Using empirical abundance patterns from young stars can have a significant impact on predicted flux ratios, particularly when attempting to describe the range of observed flux ratios in galaxies ([Nicholls et al. 2017](#)). Additionally, most published ionization model libraries do not holistically account for the effects of dust on gas, instead simply offsetting the carbon abundance relative to oxygen to account for depletion onto grains (e.g., [Gutkin et al. 2016](#)). A complete, empirical treatment of dust depletion can affect the gas phase abundance patterns of many elements (notably carbon, silicon, and iron) and the dust content of the gas. The dust and gas content directly affects cooling by line emission from metals, heating by ionization and the photoelectric effect, and the rate at which ionizing energy is absorbed by the gas (e.g., [Dopita et al. 2002](#); [Groves et al. 2004](#)). All of these effects have implications for the temperature, density, and ionization structure of model nebulae.

We present a new, uniformly implemented and empirically motivated library of ionization models to explore shocks as an alternative explanation for the observed C III], C IV, N III, N IV], O III], and He II emission lines. In §2, we explain our suite of ionization models computed using the MAPPINGS V code ([Sutherland & Dopita 2017](#); [Sutherland et al. 2018](#)), the fully empirical abundance patterns from [Nicholls et al. \(2017\)](#) and dust depletion scheme from [Jenkins \(2009, 2014\)](#), and the latest atomic data from CHIANTI ([Del Zanna et al. 2021](#)). Our approach ensures that the only differences among our predictions are the ionization mechanisms. We compile observations of nitrogen-excess galaxies from the literature, which we review in §3, for comparison with these models. We use our new suite of models to assess new and existing emission line flux ratio diagrams to classify the nitrogen-excess galaxies at $z > 5$ in §4 and find we can largely account for the apparent excess with shock excitation. Then, we discuss the implications for nitrogen abundances and high redshift ISM conditions in §5, including corroborating evidence for shocks, reduction in measured nitrogen excess, and how Wolf Rayet stars may lead to the unique conditions we observe.

2 A LIBRARY OF UNIFORMLY TREATED MODELS

Here, we present our new library of ionization models, which have uniformly implemented empirical abundance patterns and dust depletion treatment as well as updated atomic data. To date, no library of ionization models has been established on homogeneous foundations, which introduces possible systematic differences in both assumptions and approaches to numerical solutions and makes them unsuitable for this investigation. We take this homogeneous approach, drawing on empirical trends and physically-motivated inputs to build our library. To ensure uniformity across our models, we make consistent use the [Nicholls et al. \(2017\)](#) empirical stellar abundance patterns scaled by the ζ_{O} parameter (analogous to Z/Z_{\odot}) for $\zeta_{\text{O}} = 0.05$ to 2 (roughly 5 to 200% Z/Z_{\odot}), the [Jenkins \(2009, 2014\)](#) empirical dust depletion scheme with $F_{\star} = 0.43$ (30% of carbon, 80% of silicon, and 97% of iron are locked into dust grains) when dust is applicable, and the MAPPINGS V code (v5.2.1, [Sutherland & Dopita 2017](#); [Sutherland et al. 2018](#)) with atomic data from the CHIANTI database (v10, [Del Zanna et al. 2021](#)) applied to all types models. For robustness in distinguishing between ionization sources, we consider photoionization

by an AGN or by stellar populations and collisional ionization by shocks. We list the specific model parameters in Table 1.

2.1 Photoionization

Perhaps the most fundamental assumed component of photoionization models is the ionizing photon spectral energy distribution (SED), which is the key distinction between stellar and non-stellar photoionization.

For SFGs, we consider two sets of model ionizing photon SEDs, assuming in both cases a [Kroupa \(2001\)](#) IMF with a $120 M_{\odot}$ cutoff. For the first set, we use Starburst99 ([Leitherer et al. 1999, 2014](#); [Levesque et al. 2012](#)), selecting the Geneva isochrones accounting for stellar rotation ([Ekström et al. 2012](#); [Georgy et al. 2013](#)) and the WM-Basic ([Pauldrach et al. 1998](#)) and CMFGEN ([Hillier & Miller 1998, 1999](#)) atmospheres, interpolating over the predicted SEDs to approximately match the [Nicholls et al. \(2017\)](#) abundance patterns following [Dopita et al. \(2013\)](#). To allow for evolution of extragalactic H II regions (cf. [Dopita et al. 2005, 2006](#)), we choose single populations with ages of 1, 3, 5, 7, and 10 Myr as well as a continuous star formation scenario with 50, 100, 150, 200, and 300 Myr. For the second set, we use BPASS ([Byrne et al. 2022](#)), which incorporates the effects of binary stars. Again accounting for possible evolution, we consider single populations with ages of 3, 5, and 7 Myr and continuous star formation with 50 to 250 Myr durations in 50 Myr intervals.

For AGN, we consider a disk-powerlaw SED as predicted by the OPTX AGNF code ([Thomas et al. 2016](#)) and the [Jin et al. \(2012\)](#) multicolored blackbody with cool and hot inverse-Compton scattering components. These SEDs are parameterized by the black hole mass (10^4 to $10^7 M_{\odot}$) and accretion rate as a fraction of Eddington luminosity (0.01 and 0.3) and include a non-disk (i.e., non-thermal) power law component ($L\nu \propto \nu^{-\alpha}$) with an index of $\alpha = 2.2$ ([Dopita et al. 2014](#); [Thomas et al. 2016](#)).

Following previous investigations (e.g., [Dopita et al. 2002](#); [Groves et al. 2004](#); [Davies et al. 2016](#); [Thomas et al. 2016](#); [Zhu et al. 2023](#)), we incorporate full treatment of dust and radiation pressure assuming an isobaric density profile for all photoionization models, which can well-approximate conditions in AGN and SFGs with complex gas geometries (cf. [Dopita et al. 2002](#); [Groves et al. 2004](#); [Kewley et al. 2019](#)). For SFGs, we also consider an isochoric density profile, which may be justified in the cases of larger and/or more evolved H II regions ionized by stars (e.g., [Phillips 2008](#)). For reference and illustrative purposes, we also include isochoric density profiles for a subset of our AGN models, although the effects on our proposed diagnostics are marginal (cf. comparison of AGN models in [Zhu et al. 2023](#)). We note that some AGN narrow-line regions (NLRs) can be described by a powerlaw density profile (e.g., [Binette et al. 2024](#), [Flury et al. in prep](#)); however, this scenario is beyond the current scope of our investigation and should not impact the proposed diagnostic regimes since, even at high initial densities, the power law profile line predictions are still consistent with the low-density limit for collisionally excited lines like O III] and N III] (e.g., [Binette et al. 2024](#), [Flury et al. in prep](#)).

To illustrate the power of emission lines of various ions in diagnosing photoionization excitation mechanisms, we compare ionizing photon SEDs from a subset of AGN and SF models in Figure 1 with notable ionization potential energies listed in Table 2. While similarities between the AGN and SFG ionizing photon SED shapes exist at wavelengths higher than $\sim 228 \text{ \AA}$, they diverge dramatically below this threshold. This difference arises from the He I photoionization optical depth in stellar atmospheres and the Wein tail of the stellar

Table 1. Model grids computed using MAPPINGS V v5.2.1 (Sutherland & Dopita 2017; Sutherland et al. 2018) with the CHIANTI atomic data (Del Zanna et al. 2021) using the Nicholls et al. (2017) empirical abundance patterns of $\zeta_{\text{O}} = 0.05$ to 2 (roughly 5 to 200% Z/Z_{\odot}). We implement the Jenkins (2009, 2014) empirical dust depletion scheme where dust is applicable, assuming $F_{\star} = 0.43$ such that 30% of carbon, 80% of silicon, and 97% of iron are locked into dust grains. For isochoric photoionization models (including the shock precursors) we cover a grid in density from 10 to 10^4 cm^{-3} (1 to 10^5 cm^{-3} in the case of shocks). For isobaric models, we cover a grid in P/k from 10^5 to 10^9 K cm^{-3} .

Ionization Source	Ionization Strength	Parameters	Density Structure
BPASS v2.2 (Byrne et al. 2022)	$\log U = -4$ to -0.5	3 to 7 Myr inst, 50 to 250 Myr cont	isobaric or isochoric
STARBURST99 (Leitherer et al. 1999, 2014)	$\log U = -4$ to -0.5	1 to 7 Myr inst, 50 to 300 Myr cont	isobaric or isochoric
Jin et al. (2012) AGN SED	$\log U = -4$ to -1	$M_{\text{BH}} = 10^6$ to $10^7 M_{\odot}$, $L/L_{\text{Edd}} = 0.01, 0.3$	isobaric
Thomas et al. (2016) OPTXAGNF AGN SED	$\log U = -4$ to -0.5	$M_{\text{BH}} = 10^4$ to $10^7 M_{\odot}$, $L/L_{\text{Edd}} = 0.01, 0.3$	isobaric or isochoric
radiative shock + bremsstrahlung precursor	$v_s = 50$ to 1000 km s^{-1}	$B = 10^{-4}, 0.1, 1, 10 \mu\text{G}$	isobaric isochoric
dusty radiative shock + bremsstrahlung precursor	$v_s = 50$ to 200 km s^{-1}	$B = 10^{-4} \mu\text{G}$	isobaric isochoric

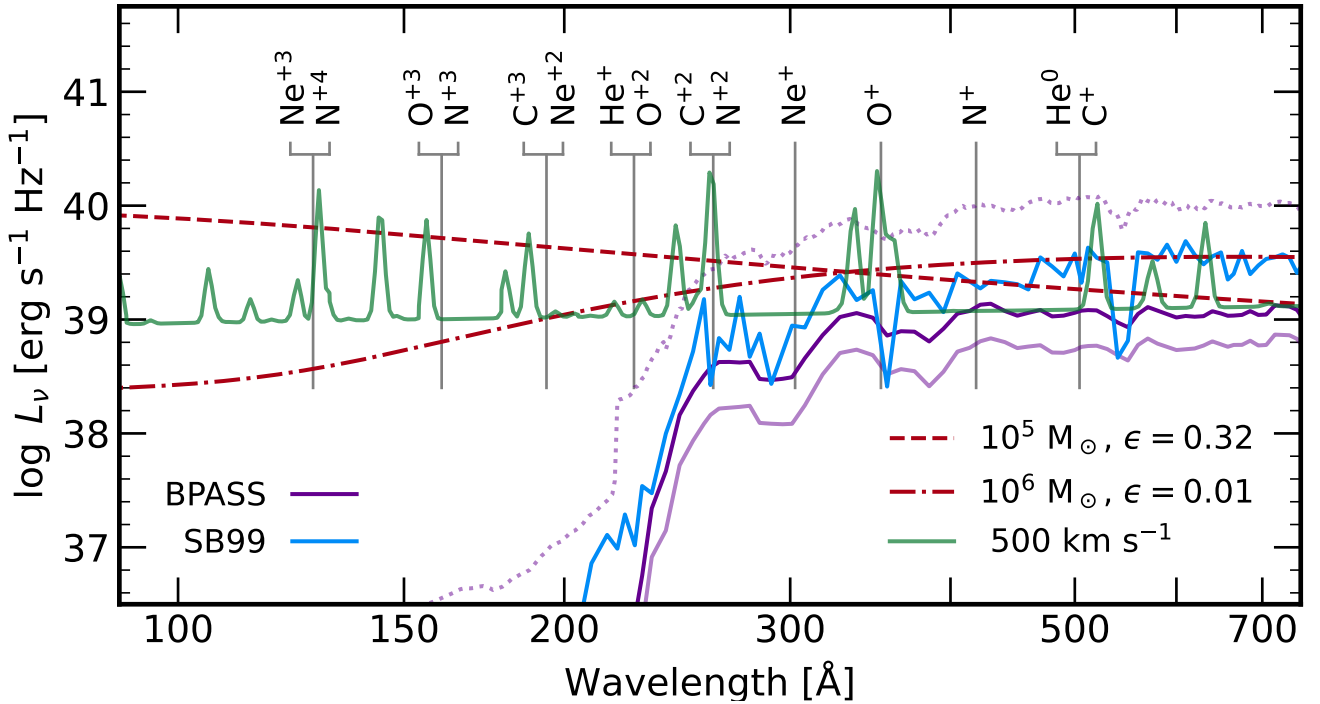


Figure 1. Ionizing photon spectral energy distribution models for oxaf disk-powerlaw AGN (Thomas et al. 2016, red), stellar populations (blue and purple), and a shock precursor (green). AGN models here indicate combinations of MBH mass and Eddington accretion rate. Stellar populations include instantaneous (solid blue and purple lines) and continuous (dotted purple line) for Starburst99 (Leitherer et al. 1999, 2014; Levesque et al. 2012, blue) and BPASS (Byrne et al. 2022, purple). MAPPINGS V upstream ionizing spectrum consisting of bremsstrahlung continuum plus X-ray cooling lines shown in green for a 500 km s^{-1} shock, scaled for visibility. Ionization potential energies of various ions are labeled and indicated by grey lines (see Table 2). The difference in ionizing photon SED becomes most pronounced blueward of 228 \AA , corresponding to the ionization potentials for He^+ and O^{+2} . The nearby C^{+2} and N^{+2} ionization potentials at 263 \AA make these ions sensitive to the differences as well due to their photoionization cross-sections.

blackbody at $T \sim 35 \text{ kK}$, effects which are not observed in characteristic AGN continua (e.g., Jin et al. 2012; Stevans et al. 2014). Thus, nebular emission from species with ionization potentials greater than the energy corresponding to the He^+ edge can readily distinguish the type of photoionizing source. As a result, He II is an excellent discriminator between AGN and SFGs when paired with, e.g., O III . Ions with photoionization cross sections which are still relatively large at this threshold will also differentiate between these excitation mechanisms. Under this criterion, C IV or N IV can be sensitive diagnostics when paired with C III or N III since C^{+2} and N^{+2} share

an ionization potential and have substantial photoionization cross sections below 228 \AA (see, e.g., Verner et al. 1996).

2.2 Shocks

Compact star-forming galaxies like those at high redshift are known to exhibit high-ionization shock signatures such as $[\text{O IV}] \lambda 25.89 \mu\text{m}$ and $[\text{Ne V}] \lambda 3426$ (e.g., Izotov et al. 2021). Ambiguously classified galaxies in the BPT can also exhibit low-ionization shock-sensitive features like $[\text{S II}] \lambda \lambda 4068, 74$ (e.g., Einsig et al. in prep, Dopita et al. e.g., 2015) and $[\text{O I}] \lambda 6300$ (e.g., Allen et al. 2008; Dopita et al.

2015) which can distinguish shock ionization from other excitation mechanisms. Shocks may significantly affect the conditions in nebulae, including ionization structure and gas density, and have been reported in AGN (e.g., Dopita 1995; Dopita et al. 2015; Dors et al. 2021; Riffel et al. 2021, Flury et al. in prep), galactic winds (e.g., Ho et al. 2014; Medling et al. 2015), mergers (e.g., Rich et al. 2011, 2015), and supernovae (e.g., Dopita et al. 2016).

Within MAPPINGS V, the shock model is treated as a time-dependent flow in the frame of the shock (e.g., Binette et al. 1985, in particular Sutherland et al. 1993 Fig 1-3 & Table 4, Allen et al. 2008 Fig 3 and §4, Sutherland & Dopita 2017 Fig 6), which we summarize here. The gas upstream of the shock has a given composition, ionization balance, density, and temperature. This gas (called the “precursor”) then flows downstream into a discontinuity described by the Rankine-Hugoniot jump conditions, the so-called shock front, and characterized by a shock velocity v_s and magnetic field strength B . After entering the shock front, the gas rapidly reaches collisional ionization equilibrium at very high temperatures ($T_s \propto v_s^2$ from conservation of energy, with $T_s \gtrsim 10^5$ K for $v_s \gtrsim 100$ km s⁻¹, e.g., Binette et al. 1985; Draine & McKee 1993; Sutherland & Dopita 2017) with exact conditions dependent on the pre-shock gas properties. The hot gas cools via bremsstrahlung radiation and line emission in the soft X-rays (e.g., Allen et al. 2008; Sutherland & Dopita 2017) in is approximately isobaric (e.g., Draine & McKee 1993; Sutherland et al. 1993). After bremsstrahlung radiation sufficiently reduces the gas temperature below $\sim 10^6$ K, additional line emission mechanisms increase the cooling efficiency to rates much higher than the recombination rate, leading to a rapid (potentially catastrophic, e.g., Falle 1975, 1981; Smith 1989) decline in temperature. A consequence of this rapid cooling is that high ionization species like Ne⁺⁴, produced by ionization energies ≥ 97.190 eV ($\sim T = 10^6$ K), persist in the radiative regime even as the gas approaches 10^4 K. Once the cooled ionized gas begins to recombine, the bremsstrahlung radiation from the hot gas within the shock (now downstream of the discontinuity) produces and sustains a photoionized region out to an ionization front which trails the shock front and which can produce secondary (albeit radiatively negligible, e.g., Sutherland et al. 1993) shocks.

In addition to the flow solution, shock models must be treated self-consistently, i.e., the ionizing spectrum produced by bremsstrahlung radiation from the hot gas within the shock travels upstream into the pre-shock gas conditions since these conditions determine properties of the gas immediately after the shock front (e.g., Shull & McKee 1979; Sutherland et al. 1993; Draine & McKee 1993; Dopita & Sutherland 1996). At $v_s \gtrsim 40$ km s⁻¹, heating of the pre-shock gas becomes important while ionization of the pre-shock gas becomes important at $v_s \gtrsim 80$ km s⁻¹ (Sutherland & Dopita 2017, their Figures 4-5). In cases of high shock velocity ($v_s \gtrsim 200$ km s⁻¹), the pre-shock gas can be sufficiently ionized by the emergent bremsstrahlung radiation that it reaches photoionization equilibrium, behaving like an H II region and even dominating the emergent nebular line emission (e.g., Binette et al. 1985; Allen et al. 2008; Sutherland & Dopita 2017). As such, incorporating these pre-shock conditions into the shock is essential. To ensure self-consistency, we adopt the iterative shock-precursor scheme introduced for MAPPINGS by Allen et al. (2008), improved upon Sutherland & Dopita (2017), and further discussed in Alarie & Morisset (2019) to account for effects of the heating and ionization of the precursor on the subsequent shock. The approach is implicit to MAPPINGS V with dramatic improvements to, among other things, treatment of the shock ionizing spectrum, precursor structure, and radiative cooling (Sutherland & Dopita 2017). MAPPINGS V computes an initial isobaric shock model under the

Rankine-Hugoniot jump conditions, predicting an emergent ionizing spectrum, the “upstream” ionizing SED (see Figure 1), which the code uses to compute a photoionization model for an isochoric one-sided slab (Sutherland et al. 1993; Sutherland & Dopita 2017; Allen et al. 2008), the “precursor”, to obtain the pre-shock ionization balance and gas temperature. MAPPINGS V recomputes the shock models assuming the precursor ionization balance and temperature for the initial conditions, generating a new upstream SED for the precursor photoionization model. We enforce a minimum of 5 iterations of this calculation as suggested in the literature (Allen et al. 2008; Sutherland & Dopita 2017; Alarie & Morisset 2019) until the preshock temperature and ionization balance converge.

Due to the extreme temperature of the gas immediately after the shock front, the dust grains can be destroyed—via thermal (gas-grain collisions) and non-thermal (betatron acceleration) sputtering for smaller grains or shattering (grain-grain collisions) for larger grains—before the shocked gas enters the radiative phase (e.g., Draine & McKee 1993; Borkowski & Dwek 1995; Jones et al. 1996). As such, we assume all of the dust grains are destroyed by the shock and thus do not consider the effects of dust in the majority of our shock models, a common convention in the literature (e.g., Allen et al. 2008; Sutherland & Dopita 2017; Alarie & Morisset 2019). To demonstrate possible effects of dust, we compute an additional set of shock models under conditions conducive to dust survival: (i) low gas temperatures after the shock front ($v_s \leq 200$ km s⁻¹, recalling $T_s \propto v_s^2$) to mimic conditions limiting thermal sputtering and grain shattering plus (ii) no magnetic field ($B = 0 \mu\text{G}$), which eliminates non-thermal sputtering.

We compute shock models across a grid of velocities v_s (50 to 1,000 km s⁻¹), densities (1 to 10^5 cm⁻³), and magnetic field strengths (10^{-4} to $10 \mu\text{G}$). To obtain the predicted shock+precursor fluxes, we take the sum of the predicted shock and precursor line fluxes, weighted by the predicted H β flux to account for the relative contributions of each component to the emergent spectrum.

3 ANCILLARY OBSERVATIONS

The aim of this study is to characterize the nitrogen excess recently reported in galaxies at $z \gtrsim 5$ using our library of ionization models based on homogeneous assumptions and implementations instead of drawing on novel physical explanations. We assemble a sample of nitrogen-excess galaxies from the literature. For context, we complement these high-redshift JWST results with nearby ($z < 0.1$) objects and a $z \sim 2$ lensed galaxy, all with N IV] and/or N III] emission reportedly due to nitrogen excess.

Several galaxies exhibiting nitrogen excess at high redshift are introduced in §1, including GHZ2 ($z = 12.4$, Castellano et al. 2024), GN-z11 ($z = 10.6$, 3 pixel extraction, high resolution gratings Bunker et al. 2023), CEERS-1019 ($z = 8.678$, Marques-Chaves et al. 2024), and GS 3073 ($z = 5.55$, $0.3 \times 0.3''$ PRISM, Ji et al. 2024). In addition to these sources, we consider the galaxies RXCJ2248-ID ($z = 6.2$, Topping et al. 2024b), GS-z9-0 ($z = 9.432$, medium resolution grating, Curti et al. 2024), and A173-zd6 ($z = 7.0435$, Topping et al. 2024a). For these seven sources, we compile UV nebular line fluxes for N IV] $\lambda\lambda 1483,86$, C IV] $\lambda\lambda 1548,50$, He II $\lambda 1640$, O III] $\lambda\lambda 1660,66$, N III] $\lambda\lambda 1747-54$, and C III] $\lambda\lambda 1907,09$ from the literature when reported.

For a lower-redshift complement, we include three galaxies with properties similar to those exhibiting nitrogen excess at $z > 5$. The VLT/MUSE observations of the $z = 2.329$ the Lyman continuum (LyC) leaking knot of the Sunburst Arc indicate a nitrogen excess

Table 2. Lower and upper ionization potential energies for ions traced by the emission represented in our emission line flux ratio diagnostics. Columns indicate (i) the ion, (ii) the vacuum wavelength(s) of the associated emission line(s), (iii) the energy $E_{i-1 \rightarrow i}$ necessary to produce the ion N^{+1} by removing an electron from the lower ion species N^{+i-1} , and (iv) the energy $E_{i \rightarrow i+1}$ necessary to ionize N^{+i} to the higher ion species N^{+i+1} . In the case of He^{+2} , no electrons remain, and the species cannot be further ionized. Here and throughout, the N III] $\lambda\lambda 1747, 49, 50, 52, 54$ quintuplet is expressed as $\lambda\lambda 1747-54$. Values obtained from NIST (Kramida et al. 2023).

ion	λ [Å]	$E_{i-1 \rightarrow i}$ [eV]	$E_{i \rightarrow i+1}$ [eV]
He^{+2}	1640	54.418	
C^{+2}	1548,50	24.383	47.888
C^{+3}	1907,09	47.888	64.494
N^{+2}	1747-54	29.601	47.445
N^{+3}	1483,86	47.445	77.474
O^{+}	3726,29	13.618	35.121
O^{+2}	1660,66	35.121	54.936
Ne^{+2}	3869	40.963	63.423
Ne^{+3}	2424	63.423	97.190
Ne^{+4}	3426	97.190	126.247

(Vanzella et al. 2020; Pascale et al. 2023; Welch et al. 2024). Green Pea analog Mrk 71 ($z = 0.000805$) is quite similar to the Sunburst Arc in terms of its physical ISM properties and stellar populations (e.g., Smith et al. 2023) and exhibits high temperatures and elevated $\log(\text{N}/\text{O})$ relative to trends among H II regions (e.g., Esteban et al. 2002, 2009). Nearby ($z = 0.00547$) galaxy Mrk 996 has a reported nitrogen excess accompanied by strong Wolf-Rayet features indicative of enrichment in action (Thuan et al. 1996, 2008; James et al. 2009; Telles et al. 2014). This blue dwarf compact star-forming galaxy has been considered as an analog to nitrogen-excess galaxies at the epoch of reionization (Senchyna et al. 2023; Marques-Chaves et al. 2024) and may help to provide local insight into the nature of the higher redshift populations. We use the recent, more sensitive *HST*/COS observations of Mrk 996 from the COS Legacy Archive Spectroscopic Surveys (CLASSY Berg et al. 2022; Mingozi et al. 2022). Together, Mrk 71, Mrk 996, and the Sunburst Arc provide our lower redshift complement the nitrogen-loud galaxies at $z > 5$. We also include 5 extreme ionization sources at $z \sim 0$ analogous to high-redshift C IV emitters from Jung et al. (2024) as these galaxies purportedly exhibit some contribution from shocks and are similar to the shock-excited [Ne V] $\lambda 3426$ emitters from Izotov et al. (2021). To provide context for these extreme galaxies, we compare these extreme objects with a more complete sample of nearby ($z \sim 0$) SFGs from CLASSY (Berg et al. 2022; Mingozi et al. 2022) as a reference and foundation for our diagnostics.

4 RESULTS

We consider two classes of emission lines based on the critical densities of the upper states of their transitions, which we have determined using PyNeb (Luridiana et al. 2015) and listed in Table 3. i) those which have high critical densities, including C IV $\lambda\lambda 1548, 50$, He II $\lambda 1640$, O III] $\lambda\lambda 1660, 6$, N III] $\lambda\lambda 1747-54$ quintuplet, and [Ne III] $\lambda 3869$, making them excellent ionization, temperature, and abundance diagnostics, and ii) those which have low critical densities, including the [N IV] $\lambda 1483$ and [C III] $\lambda 1907$ lines and the [O II] $\lambda\lambda 3726, 9$ doublet, making them excellent probes of gas density and shock excitation, particularly N IV] and C III] in the cases where post-shock densities can be relatively high ($\gtrsim 10^4 - 10^5 \text{ cm}^{-3}$). We

Table 3. Sensitivity of various emission lines to electron density. Columns indicate (i) line species, (ii) the vacuum wavelength(s), (iii) the upper state of the electronic transition producing the line via spontaneous emission, and (iv) critical densities n_c of the upper state. We calculate n_c using PyNeb (Luridiana et al. 2015) assuming $T_e \sim 10^4$ K. Increasing T_e results in a slight increase in n_c .

species	λ [Å]	upper state	n_c [cm^{-3}]
[N IV]	1483	$^3\text{P}_2$	10^5
N IV]	1487	$^3\text{P}_1$	4×10^9
C IV	1548,50	^2P	10^{15}
O III]	1660,66	$^5\text{S}_2$	4×10^{10}
N III]	1747-54	^4P	10^{10}
[C III]	1907	$^3\text{P}_2$	7×10^4
C III]	1909	$^3\text{P}_1$	10^9
[O II]	3726	$^2\text{D}_{3/2}$	8×10^3
[O II]	3729	$^2\text{D}_{5/2}$	3×10^3
[Ne III]	3869	$^1\text{D}_2$	10^7

further consider in the construction of our diagnostics the ionizing energy of the ions associated with each of the emission lines, which we list in Table 2. The C IV $\lambda\lambda 1548, 50$ doublet, while promising due to its ionization potential and high critical density, can suffer from stellar contamination (as in Mrk 71, e.g., Smith et al. 2023), which may complicate its use as a nebular diagnostic (e.g., Mingozi et al. 2024).

Since our aim is to understand the ionization mechanisms and related nitrogen abundance in galaxies at $z > 5$, we limit our considered predictions to those for models of $\zeta_{\text{O}} \leq 0.5$ ($12 + \log(\text{O}/\text{H}) \leq 8.35$) to avoid accounting for observed flux ratios with unrealistically high metallicities. We also confirm that our models predict [O III] $\lambda 5007$ / $\text{H}\beta$, [N II] $\lambda 6584$ / $\text{H}\alpha$, [S II] $\lambda\lambda 6716, 31$ / $\text{H}\alpha$, and [O I] $\lambda 6300$ / $\text{H}\alpha$ flux ratios within the typical range of Veilleux & Osterbrock (1987) BPT diagnostics.

4.1 Previous Diagnostics for $z > 5$

4.1.1 C III], C IV, and He II

First proposed by Villar-Martin et al. (1997), diagnostics based on C III], C IV, and He II rely predominantly on the differences in the C^+ , C^{+2} , and He^+ ionization potentials to distinguish between AGN and SFGs using C III]/He II, although Villar-Martin et al. (1997) also demonstrate possible overlap between shocks and AGN. We show their primary diagnostic in the top panel of Figure 2. The much closer ionization potentials of C^{+2} and He^+ cause C IV/He II to provide some but less diagnostic power (see Feltre et al. 2016, their Figure 14). With our more uniform and empirically-motivated models, we find that C III] / He II is the primary discriminator between AGN and SFGs, with C IV / He II being largely insensitive to differences in photoionizing SED. We also find that C III] / He II can distinguish between shocks and photoionization by stars, in keeping with the Jaskot & Ravindranath (2016) investigation of shock contributions to C III] (grey line in Figure 2). From our models, we confirm that C IV / He II can isolate radiative shocks from a subset of the AGN models, overlapping only with model predictions of high ionization parameter. We provide definitions below for the flux ratio regimes

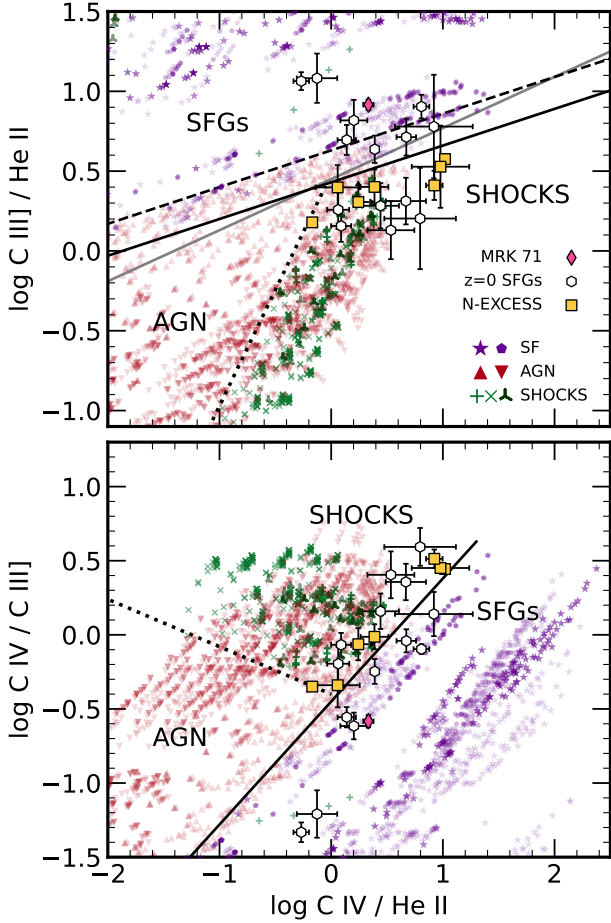


Figure 2. BPT-style diagnostics for $C\text{ III]}/\text{He II}$ (*top*) and $C\text{ IV]}/C\text{ III]}$ (*bottom*) vs $C\text{ IV]}/\text{He II}$. Our model predictions for $Z_{\odot} \leq 0.5$ ($\lesssim 50\% Z_{\odot}$) are shown in purple for SFGs (stars and pentagons for instantaneous and continuous star formation, respectively), red for AGN (up and down triangles for the [Jin et al. 2012](#) and [Thomas et al. 2016](#) SED models, respectively), and green for shocks (crosses and exes for $v_s \leq 200 \text{ km s}^{-1}$ and $v_s > 200 \text{ km s}^{-1}$, the “low” and “high” shock velocity regimes, respectively; triradii for dusty shocks with $v_s = 50\text{--}200 \text{ km s}^{-1}$). Yellow squares correspond to nitrogen-excess galaxies at $z > 5$ observed with *JWST*. Pink diamond indicates the giant extragalactic H II region Mrk 71-A, a Green Pea analog exhibiting density enhancement and signatures of massive stars. White hexagons indicate the $z \sim 0$ star-forming galaxies from CLASSY ([Berg et al. 2022](#); [Mingozi et al. 2022](#)) and from [Jung et al. \(2024\)](#). Grey line is the 10% shock mixture boundary given by [Jaskot & Ravindranath \(2016\)](#). Black lines indicate our limits for SFGs (solid), AGN (dashed), and shocks (dotted) as given by Equations 1 (*top*) and 2 (*bottom*).

for each ionization mechanism:

$$x = \log_{10} \left(\frac{C\text{ IV]}}{\text{He II}} \right), \quad y = \log_{10} \left(\frac{C\text{ III]}}{\text{He II}} \right)$$

$$y = \begin{cases} 0.23x + 0.45, & \text{shock below, BSFG above} \\ 0.23x + 0.63, & \text{AGN below, CSFG above} \\ 1.45x + 0.48, & \text{shock below} \end{cases} \quad (1)$$

where BSFG corresponds to the instantaneous burst star-forming galaxy and CSFG corresponds to a continuously star-forming galaxy. We show these demarcations in Figure 2 as solid, dashed, and dot-

ted lines, respectively, with the [Jaskot & Ravindranath \(2016\)](#) 10% shock-SFG mixing sequence for reference.

As evidenced by their location in Figure 2, all seven nitrogen-excess galaxies at $z > 5$ are consistent with high ionization parameter AGN or shocks, as are several of the CLASSY SFGs and all of the extreme ionization SFGs. The location of two low-metallicity CLASSY galaxies, J0337-0502 (SBS0335-052 E) and J0934+5514 (I Zw 18 NW), and four of the five extreme ionization SFGs below the shock and SFG limits in Equation 1 may indicate that shocks are a dominant mechanism. [Mingozi et al. \(2024\)](#) find in their own UV diagnostics that the two low metallicity CLASSY galaxies are star-formation dominated with evidence for additional shock ionization, as do [Jung et al. \(2024\)](#) for the five C IV emitters. Mrk 71, known to exhibit high gas densities and stellar winds, resides squarely in the SFG locus; however, low velocity shock models with $v_s = 100$ and 150 km s^{-1} straddle the observed flux ratios.

When paired with C III], C IV] becomes a far stronger ionization diagnostic. This flux ratio is relatively insensitive to metallicity as it depends on emission from ions of the same element (see, e.g., [Mingozi et al. 2022](#), Figure 14). Thus this flux ratio less ambiguously assesses the hardness of the ionizing spectrum. Since the ionizing SEDs of AGN and stellar populations tend to diverge blueward of the C^+ ionization potential (see Figure 1), the addition of He II can provide the leverage necessary to distinguish between excitation regimes. Pairing $C\text{ IV]}/C\text{ III]}$ with $C\text{ IV]}/\text{He II}$ thus provides a clear distinction between AGN and SFG photoionization as depicted in the bottom panel of Figure 2 (see also [Zhu et al. 2023](#), their Figure 10), a distinction more pronounced than with $C\text{ III]}/\text{He II}$ vs $C\text{ IV]}/\text{He II}$ but without any additional lines. Shocks continue to occupy the same space as high ionization parameter AGN. We define the ionization regimes as

$$x = \log_{10} \left(\frac{C\text{ IV]}}{\text{He II}} \right), \quad y = \log_{10} \left(\frac{C\text{ IV]}}{C\text{ III]}} \right)$$

$$y = \begin{cases} 0.83x - 0.45, & \text{SFG below, shock \& AGN above} \\ -0.32x - 0.40, & \text{shock above} \end{cases} \quad (2)$$

We show these demarcations in the bottom panel of Figure 2.

As with $C\text{ III]}/\text{He II}$ vs $C\text{ IV]}/\text{He II}$, the seven nitrogen excess galaxies at $z > 5$ reside just within the boundaries for the shock excitation regime but may also be consistent with high ionization AGN (see Figure 2). Interestingly, [Topping et al. \(2024a\)](#) classified A1703-zd6 and RXCJ2248-ID as consistent with SFG models when using $C\text{ III]}/C\text{ IV]}$ and previous photoionization models based on scaled-solar abundance patterns. Accounting for a more robust and updated abundance pattern set combined with empirical dust depletion, we find that $C\text{ III]}$, $C\text{ IV]}$ consistently places both A1703-zd6 and RXCJ2248-ID just above the maximal SFG demarcation, as shown in Figure 2 as well as in other diagnostics containing $C\text{ III]}/C\text{ IV]}$ (e.g., Figure 3). Not only does this difference speak to the significance of using appropriate abundance patterns to define flux ratio diagnostic spaces but also indicates that these two galaxies’ nebular emission may be contaminated or even dominated by shocks.

Again, CLASSY galaxies J0337-0502 and J0934+5514 and the same four shock-contaminated [Jung et al. \(2024\)](#) SFGs fall within the shock excitation regime, albeit rather close to the demarcation for SFGs. Although residing in the SFG regime, Mrk 71 is also close to the demarcation. Together, the $C\text{ IV}$, $C\text{ III]}$, $O\text{ III]}$, and He II emission from these seven local SFGs suggests that shocks could describe the line ratios of the nitrogen-bright galaxies at high redshift. Similar $C\text{ IV}$ emitters at the epoch of reionization may be associated with shocks, likely indicating feedback from massive stars. That being

said, a diagnostic more sensitive to shock excitation is necessary to distinguish whether AGN or shocks are responsible for the observed emission in nitrogen-excess galaxies.

4.1.2 $C\text{ III}]$, $C\text{ IV}$, and He II with $\text{O III}]$

The most fundamental shortcoming of the $C\text{ IV}/\text{He II}$ and $C\text{ III}]/\text{He II}$ vs $\text{O III}]/\text{He II}$ diagnostics is that, given both axes are normalized to He II , the flux ratios are extremely sensitive to metallicity (the C/O ratio, e.g., Jaskot & Ravindranath 2016; Gutkin et al. 2016) and the preferential depletion of carbon into dust grains relative to oxygen (e.g., Gutkin et al. 2016) in addition to ionization parameter. We find this sensitivity to be the case in our model predictions as well, limiting the extent to which these paired flux ratios can function as an ionization diagnostic.

For $C\text{ IV}$, the exceptionally high critical densities of the 2P states mitigates any effects of shocks on the line diagnostics. As a result, $C\text{ IV}/\text{He II}$ is more sensitive to the precursor photoionized by the shock emission than $C\text{ III}]/\text{He II}$. Given the similarities between the AGN and shock bremsstrahlung SEDs in Figure 1, $C\text{ IV}$ should not distinguish well between shocks and high ionization AGN, which is consistent with the results in Figure 3. As shock velocity decreases, so does the peak of the emergent ionizing SED, making the precursors of lower velocity shocks appear similar to high ionization SFGs, further diminishing the ability of $C\text{ IV}/\text{He II}$ to distinguish shocks from other ionizing mechanisms. However, $C\text{ IV}$ and He II together trace the stark differences in AGN and stellar SEDs between 200 and 300 Å. Since $\text{O III}]$ and He II are similarly sensitive to the drop ion stellar ionizing SEDs, it is perhaps no surprise that $C\text{ IV}/\text{He II}$ vs $\text{O III}]/\text{He II}$ provides one of the best demarcations between AGN and SFG photoionization among the diagnostics considered in the literature. We define demarcations between AGN and SFGs such that

$$x = \log_{10} \left(\frac{\text{O III}]}{\text{He II}} \right), \quad y = \log_{10} \left(\frac{C\text{ IV}}{\text{He II}} \right) \quad (3)$$

$$y = \begin{cases} 2.33x - 0.37, & \text{SFG below, AGN above} \\ 0.58x - 0.24, & \text{shock above} \end{cases}$$

and

$$x = \log_{10} \left(\frac{\text{O III}]}{\text{He II}} \right), \quad y = \log_{10} \left(\frac{C\text{ IV}}{C\text{ III}]} \right)$$

$$y = \begin{cases} 3.75 \left(1 + e^{-2.20x} \right)^{-1} - 2.73, & \text{SFG below, shock \& AGN above} \\ -0.35x - 0.38, & \text{shock above} \end{cases} \quad (4)$$

which we show in the top and bottom panels of Figure 3 with solid and dotted lines, respectively.

We find the effects of shock compression on the $[C\text{ III}]$ line can serve to further separate the shock models from those of AGN with high ionization parameter, a result of the four orders of magnitude difference in critical density between the $\text{O III}]$ transitions and $[C\text{ III}] \lambda 1907$ (see Table 3). Perhaps most compelling about this result is that the seven $z > 5$ nitrogen-excess galaxies either reside in the shock locus of this diagnostic or within uncertainties could readily occupy it. The CLASSY SFGs and our nitrogen-excess analogs occupy a sequence extending from the shock regime into the heart of the SF locus, with uncertainties allowing for the majority of SFGs to occupy either ionization regime. While Mrk 996 does not appear to be shock excited according to the Mingozi et al. (2024) demarcation, this galaxy, Mrk 71, and the Sunburst arc could be explained by lower

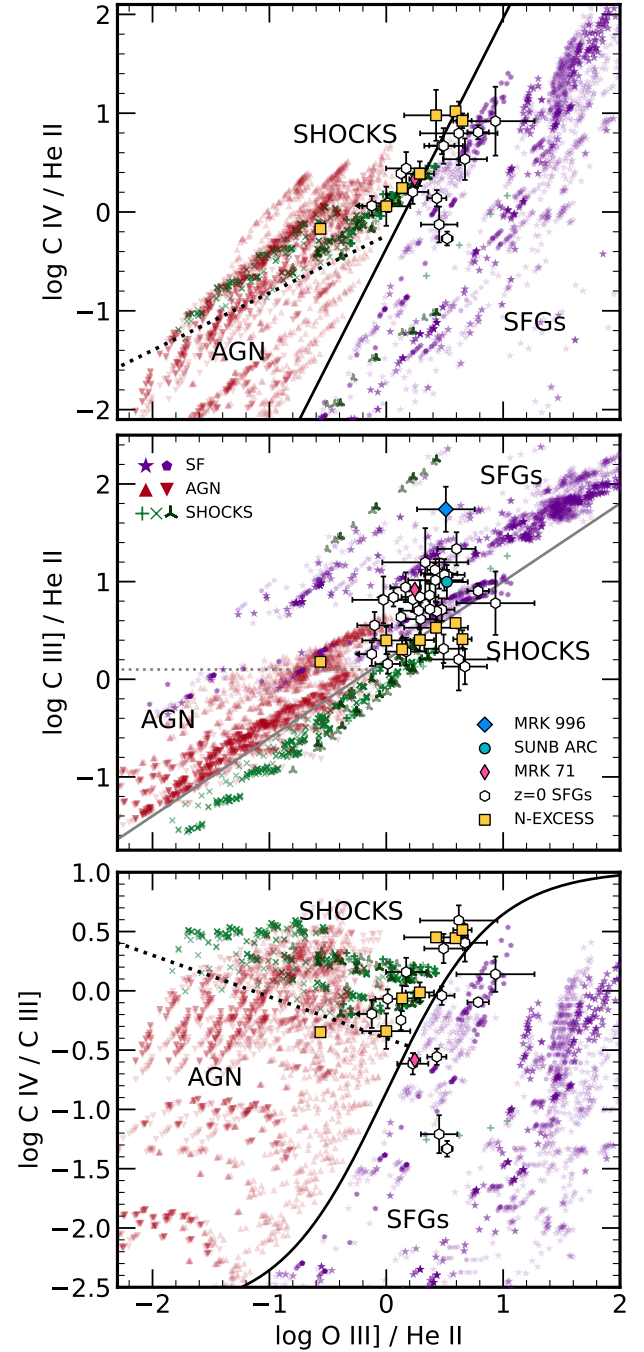


Figure 3. BPT-style diagnostic for $C\text{ IV}/\text{He II}$ (top), $C\text{ III}]/\text{He II}$ (center), and $C\text{ IV}/C\text{ III}]$ (bottom) vs $\text{O III}]/\text{He II}$. Symbols as in Figure 2. Blue diamond indicates the low-redshift galaxy Mrk 996 exhibiting nitrogen excess and signatures of massive stars. Cyan circle indicates the nitrogen-excess knot of the Sunburst arc ($z = 2.39$) exhibiting winds and Lyman continuum escape. Solid and dotted black lines in the top and bottom panels indicate demarcations given by Equations 3 and 4, respectively. Solid and dotted grey lines in the center panel indicate demarcations from Mingozi et al. (2024).

density ($n_{\text{H}} = 1 \text{ cm}^{-3}$) shock models with $v_s = 50$ to 100 km s^{-1} . Alternatively, mixing of the SFG and shocks within the COS aperture could be pushing these galaxies toward the demarcation (see shock-SF mixing explored for other diagnostics in [Jaskot & Ravindranath 2016](#)).

We note that the distinction between AGN, SFGs, and shocks only holds at low metallicity. Expanding to high metallicities causes the shock models to occupy a portion of the SFG locus where our local nitrogen-excess reference objects reside, as well as a significant portion of the CLASSY galaxies. Further complications include the substantial overlap between AGN and SFG model predictions. The putative AGN GS 3073 resides in an ambiguous part of the diagnostics, offset from other nitrogen-excess galaxies due to a relatively weak $\text{O III}]$ emission relative to He II . While enhanced He II is a possible signature of AGN activity, we cannot rule out a scenario such as SFG-shock mixing, leaving confirmation of the presence of an AGN to other diagnostics.

In general, $\text{C III}] / \text{He II} + \text{O III}]$ vs $\text{O III}] / \text{He II}$ can differentiate between pure shocks and other mechanisms at low metallicity. We attribute this ability to collisional suppression of $[\text{C III}] \lambda 1907$ and augmentation of $\text{O III}] \lambda \lambda 1660, 66$. While He II is a strong discriminator of SFGs due to the He^+ ionization potential, sufficient similarities in AGN and SFG ionizing SEDs at the ionization potentials of O^+ and C^+ limit the diagnostic power of $[\text{C III}] \lambda \lambda 1907, 09$ and $\text{O III}] \lambda \lambda 1660, 66$ for photoionization sources.

4.1.3 $[\text{Ne III}]$ and $[\text{O II}]$

The $[\text{Ne III}] \lambda 3869 / [\text{O II}] \lambda \lambda 3726, 9$ ratio is purported to distinguish between various excitation mechanisms (the so-called ‘‘OHNO’’ diagram, [Backhaus et al. 2022](#)). We have explored $[\text{Ne III}]/[\text{O II}]$ and find that this flux ratio, while a good probe of ionization parameter (see, e.g., [Levesque & Richardson 2014](#)), does not discriminate between excitation mechanisms (see similar results in [Zhu et al. 2023](#)). We attribute this lack of diagnostic power to the similar shapes of ionizing SEDs at these ionization potential energies (Figure 1).

4.2 A Low-Resolution Rest-UV Diagnostic for $z > 5$

Of-employment emission line flux ratio diagnostics (notably the BPT [Baldwin et al. 1981](#); [Veilleux & Osterbrock 1987](#)) are designed with two observational limitations in mind: (i) detectability of the line, including resolution from adjacent features, and (ii) sensitivity to extinction. As such, lines considered must not only meet the scientific objectives outlined above but also satisfy the observational restrictions. Namely, lines must be bright and close in wavelength to limit the *relative* effects of extinction while being sufficiently separated to be resolved by conventional spectrographs. In the lattermost case, the low resolutions of *JWST*/NIRSpec PRISM/CLEAR at $z > 3$ and *HST*/STIS G230L at $z < 0.5$ can complicate the use of various diagnostics. Features like He II and $\text{O III}]$ will often be blended and difficult to separate accurately, potentially introducing bias into how diagnostic diagrams are interpreted. Previously proposed diagnostics (e.g., [Villar-Martin et al. 1997](#); [Feltre et al. 2016](#); [Jaskot & Ravindranath 2016](#); [Mingozzi et al. 2024](#)) assume resolution of the He II and $\text{O III}]$ blend, that the 400 \AA separation between C IV and $\text{C III}]$ is insensitive to dust, or that the UV continuum is only described by the ionizing source – as is the case for all equivalent width diagnostics – despite the fact that stellar populations older than 10 Myr (i.e., non-ionizing) can still contribute appreciably to the FUV continuum without affecting the ionizing continuum (e.g., [Chisholm et al. 2019](#)).

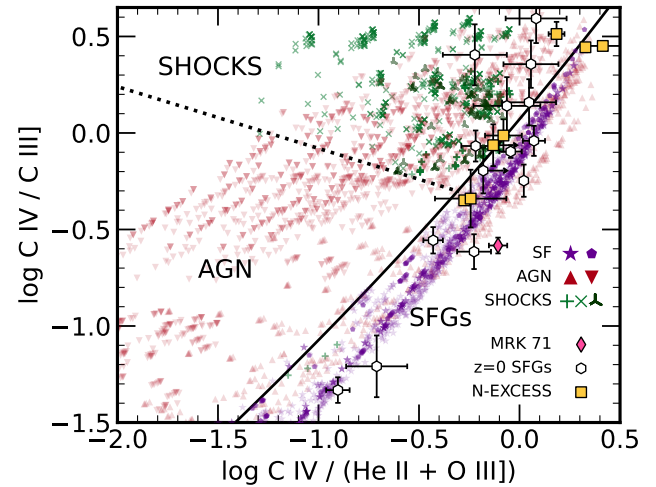


Figure 4. BPT-style diagnostics for $\text{C IV}/\text{C III}]$ vs $\text{C IV}/(\text{He II} + \text{O III}]$. Yellow squares correspond to nitrogen-excess galaxies at $z > 5$ observed with *JWST*. Symbols as in Figure 2. Solid, and dotted lines correspond to Equation 5 to distinguish excitation regimes, which we have labeled.

With these considerations in mind, we propose a BPT-style flux ratio diagnostic that not only is motivated by previous diagnostics but also accounts for the low resolution of *JWST*/NIRSpec PRISM/CLEAR. This diagnostic compares the bright $\text{C III}]$ and C IV lines with the $\text{He II} + \text{O III}]$ blend to distinguish different flux ratio regimes explicable by SFGs, AGN, and radiative shocks. We define these regimes using maximum/minimum demarcations following previous sections such that

$$x = \log_{10} \left(\frac{\text{C IV}}{\text{He II} + \text{O III}] } \right), \quad y = \log_{10} \left(\frac{\text{C IV}}{\text{C III}] } \right)$$

$$y = \begin{cases} -(43.41 - 16.39x)^{1/2} + 6.66, & \text{SF below, shock above} \\ -0.32x + 0.4, & \text{shock above} \end{cases} \quad (5)$$

We show these demarcations in Figure 4 as solid and dotted lines, respectively.

As evident in Figure 4, the $\text{C III}]/(\text{He II} + \text{O III}]$ ratio serves primarily to distinguish between SF and AGN photoionization, with a sharp upper limit in $\text{C III}]/(\text{He II} + \text{O III}]$ for the AGN model predictions. A similar lower limit in $\text{C III}]/(\text{He II} + \text{O III}]$ exists for the star forming galaxies. While these limits overlap by ~ 0.1 to 0.3 dex, the AGN and SFG regions are otherwise distinctly separate. As with previous diagnostics considered, the nitrogen-excess galaxies reside within this overlap, making direct classification ambiguous at best. Additional diagnostics assuming higher resolution and higher sensitivity will therefore be necessary to ascertain the excitation mechanism(s) at play in the object of interest.

Shocks, while overlapping with the AGN models, occupy the upper left of Fig 4, owing primarily to collisional suppression of $\text{C III}]$. For a fixed set of parameters, varying the shock velocity from 100 to 1000 km s^{-1} leads to a decrease in $\text{C III}]/(\text{He II} + \text{O III}]$ but an increase in $\text{C IV}/\text{C III}]$. This trend arises predominantly from the ionization structure of the shock+precursor: the number of He^+ ionizing photons increases by nearly three orders of magnitude from $v_s = 100$ to 1000 km s^{-1} while those of O^+ and C^+ increase far less dramatically (cf. [Allen et al. 2008](#)), which augment the He II line substantially relative to the $\text{O III}]$ and $\text{C III}]$ doublets. As result, the $z > 5$ galaxies exhibiting nitrogen excess are most consistent with low-velocity

shocks among our shock models. If shocks are indeed responsible (at least in part) for the ambiguous classification of these galaxies, then the shock velocities must be low. However, to distinguish readily between shocks, AGN, and SFGs, a more robust diagnostic is needed, one which may require higher resolution and sensitivity than is available with *JWST*/NIRSpec PRISM/CLEAR or the *HST*/COS or /STIS -L gratings.

4.3 Insights from O III]/He II with N III] and N IV]

If higher resolution and sensitivity are attainable, more informative diagnostic lines and flux ratios can be considered. Certainly, resolving O III] from He II will provide considerable diagnostic leverage, as seen above, as will detecting the nitrogen lines linked both to various density regimes and to the apparent nitrogen excess. In Figure 5, we compare both N III]/C III] and N IV]/C III] to O III] / He II. The N III]/C III] and N IV]/C III] ratios should be relatively insensitive to metallicity at $12 + \log(\text{O}/\text{H}) \sim 7-8$ due to the enrichment pathways of nitrogen and carbon (e.g. Henry et al. 2000; Kobayashi et al. 2020; Curti et al. 2024, Arellano-Cordova et al. in prep), making these flux ratios excellent tracers of various gas conditions. Given the critical densities of their respective transitions in Table 3, N III]/C III] serves primarily as a diagnostic of dense gas. On the other hand, N IV]/C III] serves primarily as a diagnostic of ionization because, from Table 2, N⁺³ has a similar ionization potential to C⁺³. While O III]/He II is sensitive to metallicity, this ratio is also strongly dependent on ionization, tracing the extreme UV at 353 Å and 228 Å, respectively, where the ionizing capabilities of stellar populations are expected to decline precipitously while AGN and fast radiative shocks are not. Thus, O III]/He II is an excellent diagnostic for distinguishing between stellar and non-stellar ionizing sources.

In the top panel of Figure 5, we see a reduction in C III] flux relative to N III] due to shock enhancement of the gas density, causing shock models to reside in a unique flux ratio space. A similar effect is seen in the lower panel of Figure 5, albeit less pronounced given the combined effects of ionization and lower critical densities of the N IV] transitions. The AGN and star-forming galaxy models additionally reside in largely unique flux ratio spaces, making these diagrams useful diagnostics for a variety of excitation sources. The velocity gradient noted earlier persists in these diagnostics, with increasing v_S corresponding to decreasing O III]/He II, decreasing N III]/C III], and increasing N IV]/C III].

To distinguish among the various excitation regimes in Figure 5, we provide the following quantitative diagnostics for flux ratios:

$$x = \log_{10} \left(\frac{\text{O III]}}{\text{He II}} \right), \quad y = \log_{10} \left(\frac{\text{N III]}}{\text{C III]}} \right)$$

$$y = \begin{cases} \frac{-2.6}{x+3.5} - 0.6, & \text{SFG below, shock above} \\ -0.15(x - 0.32)^2 - 1.26, & \text{AGN below, shock above} \\ -1.53x - 1.5, & \text{AGN below} \end{cases} \quad (6)$$

and

$$x = \log_{10} \left(\frac{\text{O III]}}{\text{He II}} \right), \quad y = \log_{10} \left(\frac{\text{N IV]}}{\text{C III]}} \right)$$

$$y = \begin{cases} \log_{10} (12.6 + 10^{-2x+2.1}) & \text{SFG below, shock \& AGN above} \\ -\log_{10}(x + 0.10), & \text{AGN below, shock above} \\ 0.65x - 0.21, & \text{AGN below, shock above} \end{cases} \quad (7)$$

We show these demarcations in Figure 5 as dotted, solid, and dashed

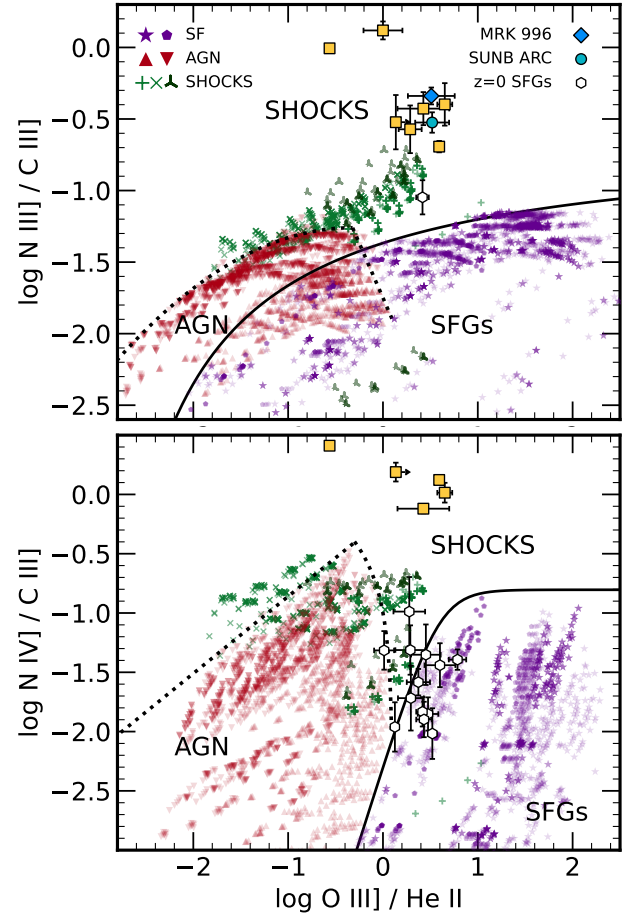


Figure 5. BPT-style diagnostics for N III]/C III] vs O III]/He II (*top*) and N IV]/C III] vs O III]/He II (*bottom*). Symbols as in Figures 2-4. Solid, dotted, and long-dashed lines correspond to Equations 6 and 7 in the top and bottom panels, respectively, to distinguish excitation regimes. The CLASSY galaxy appearing as a filled white hexagon in both panels is J1253-3012 (SHOC391). Radiative shocks occupy a unique space where extreme densities and sufficiently extreme radiation can populate the diagram above the solid, dashed, and dotted lines. The location of the high redshift galaxies in these diagnostic diagrams suggests that radiative shocks are the dominant excitation mechanism for these objects and may account for some, if not all, of the apparent nitrogen excess.

lines, respectively. N III] is noticeably better at distinguishing shocks from AGN than N IV], which we attribute to collisional suppression of the [N IV] $\lambda 1483$ line due to its comparatively low critical density.

In Figure 5, we also show observations of nitrogen-excess galaxies at $z > 5$ observed with *JWST* and compiled from the literature. Five galaxies, CEERS-1019, RXCJ2248-ID, GHZ2, GS-z9-0, and A1703-zd6, are offset from the low-velocity shock models by ≤ 0.5 dex, as are the analog galaxies Mrk 996 and the Sunburst arc. Rerunning selective cases of our shock models with a 0.5 dex increase in $\log(\text{N}/\text{O})$ brings the dust-free models into agreement with the observations. Dusty shock models require only a 0.3 dex increase in $\log(\text{N}/\text{O})$ to match these five galaxies due to effects such as radiative efficiency and depletion of C into graphitic grains. The Nicholls et al. (2017) abundance patterns for $\log(\text{N}/\text{O})$ contain a scatter of ~ 0.3 dex in the range of $12 + \log(\text{O}/\text{H})$ comprising these galaxies and our models. Therefore, the nitrogen abundance “excess” observed could

instead be an increase in flux attributable to shocks combined with a bias toward detecting brighter nitrogen lines from slightly enhanced $\log(\text{N}/\text{O})$. The $\log(\text{N}/\text{O})$ abundance in these galaxies would agree with $\log(\text{N}/\text{O})$ vs $12 + \log(\text{O}/\text{H})$ determined from Galactic stars and blue compact dwarf galaxies. Such excess could readily arise from enrichment by Wolf Rayet stars, as seen locally (e.g., [Bik et al. 2018](#); [Abril-Melgarejo et al. 2024](#)). We discuss this possibility further in §5.

One SFG from CLASSY, J1253-3012, appears in both diagrams in Figure 5 and is known to exhibit both enhanced nitrogen ($12 + \log(\text{O}/\text{H})=7.98$, $\log(\text{N}/\text{O})=-0.92$, Arellano-Cordova in prep., cf. [Guseva et al. 2011](#)) and Wolf Rayet stars (e.g., [Brinchmann et al. 2008](#); [Shirazi & Brinchmann 2012](#)). While this target was not initially considered as a possible nitrogen-excess analog, the properties of this galaxy indicate both shock excitation and high $\log(\text{N}/\text{O})$ largely consistent with the scatter in local trends from [Nicholls et al. \(2017\)](#). As with the five other shock-excited galaxies with nitrogen excess, the $\log(\text{N}/\text{O})$ excess could arise from enrichment “in action” via Wolf Rayet stars.

The two outliers, GN-z11 and GS 3073, would still require a $\gtrsim 0.8$ dex excess in $\log(\text{N}/\text{O})$ to reproduce the flux ratios using our shock models. Given possible AGN signatures in these objects ([Maiolino et al. 2024](#); [Schaerer et al. 2024](#); [Ji et al. 2024](#), respectively), particularly with the detected coronal lines in GS 3073, we propose a shock-AGN mixture where the AGN illuminates the precursor, drives a supersonic wind which shocks and compresses the gas, and prevents recombination by sustaining the post-shock radiative regime. Modeling such a scenario is beyond the scope of this paper; however, we hypothesize that the observed flux ratios arise from an AGN-shock mixture with $\log(\text{N}/\text{O})$ values similar to those of the other nitrogen-excess galaxies considered here.

5 IMPLICATIONS FOR NITROGEN

5.1 Substantiating Evidence For Shocks

We have demonstrated above that, among the models considered in this work, shocks are the only excitation mechanisms which can account for the observed $\text{N III}/\text{C III}$ and $\text{N IV}/\text{C III}$ flux ratios and are consistent with various C III , C IV , and He II flux ratios. Here, we examine evidence to support this agreement. The shock models which best describe the observations of $z > 5$ nitrogen-excess galaxies and their nearby analogs (Mrk 71, Mrk 996, and the Sunburst arc) in Figures 4 and 5 are those in the “warm partially ionized” regime described by [Sutherland & Dopita \(2017\)](#) with shock velocities $v_s \leq 200 \text{ km s}^{-1}$ ([Allen et al. 2008](#); [Sutherland & Dopita 2017](#)). Such wind velocities are observed and readily achievable in star-forming galaxies across a broad swath of cosmic time (e.g., [Steidel et al. 2010](#); [Heckman et al. 2011, 2015](#)) and can be attributed to outflows, stellar winds, and/or supernovae. Furthermore, winds in this velocity range are observed in cases of nitrogen excess at $z > 10$ (e.g., GHZ2, [Castellano et al. 2024](#)) and at lower redshift (e.g., in Mrk 996 and the Sunburst arc [James et al. 2009](#); [Rivera-Thorsen et al. 2017](#); [Vanzella et al. 2020](#); [Mainali et al. 2022](#)) and can occur even when feedback is suppressed (e.g., in Mrk 71, [Oey et al. 2017](#)). Interestingly, CLASSY galaxy J1253-3012 (SHOC391) exhibits N IV and N III in the shock regime in Figure 5 as well as wind velocities between 90 and 140 km s^{-1} (e.g., [Xu et al. 2022](#)), making it an ideal candidate for contributions from low-velocity shocks. Both the emission line diagnostics presented in Figures 4 and 5 and the kinematic evidence point to shocks as possible drivers of the line excitation.

Two CLASSY galaxies, J0337-0502 (SBS0335-052 E) and J0934+5514 (I Zw 18 NW), appear in the shock region of the C III , C IV , and He II diagrams discussed in §4.1. Both SBS0335-052 E and I Zw 18 NW exhibit strong evidence for Wolf Rayet stars (e.g., [Thuan et al. 1997](#); [Izotov et al. 1997, 2006](#)) and gas temperatures in excess of 20 kK (e.g., [Izotov et al. 2006](#)). The northern knot of I Zw 18 contains a substantial wind of ionized gas with velocities of 60-80 km s^{-1} (e.g., [Petrosian et al. 1997](#); [Arroyo-Polonio et al. 2024](#)), capable of driving low-velocity shocks consistent with its C III , C IV , He II flux ratios. I Zw 18 also exhibits a small amount of ionized gas in a superwind reaching as high as $3 \times 10^3 \text{ km s}^{-1}$ ([Arroyo-Polonio et al. 2024](#)), which may indicate suppressed stellar feedback such as in Mrk 71 (e.g., [Oey et al. 2017](#)). SBS0335-052 E exhibits similar low-velocity shocks of $\sim 100 \text{ km s}^{-1}$ in its older star-forming knots and much slower winds of 30-40 km s^{-1} in its youngest star-forming knots (e.g., [Izotov et al. 2006](#)). The slightly older star-forming regions have probably undergone supernova ([Izotov et al. 2006](#)), which could account for any low-velocity shock emission. The younger star-forming regions are likely associated with stellar winds, which would impart significantly less mechanical energy and thus drive shocks in the “warm neutral” regime of [Sutherland & Dopita \(2017\)](#) with photoionization by the earliest stars dominating the nebular emission.

5.2 Shock Heating

As discussed in §2.2, under the Rankine-Hugoniot jump conditions, gas heats up from precursor temperatures of $T \sim 10^4 \text{ K}$ to anywhere from 10^5 to 10^8 K . Because the gas does not behave isothermally, even after radiative cooling, shocked gas can maintain much higher equilibrium temperatures in excess of several tens of kK, which can augment temperature diagnostic features like the $[\text{O III}] \lambda 4363$ auroral line (e.g., [Riffel et al. 2021](#), [Flury et al. in prep](#)), particularly if magnetic fields or a paucity of metals inhibit cooling. In cases of a shock + photoionization mixture, this temperature excess can lead to severe over-estimations of the ionic emissivities due to their exponential dependence on the measured electron temperature, which in turn leads to substantial under-estimations of chemical abundances. While some observations suggest a steep decline in electron temperature between O^{+2} and lower ionization species like O^+ and N^+ (e.g., [Riffel et al. 2021](#), [Flury et al. in prep](#)), the temperature gradient in shocked gas remains empirically unconstrained. As such, the temperature relations typically invoked (e.g., [Arellano-Córdova & Rodríguez 2020](#); [Rogers et al. 2021](#)) to infer electron temperatures for ions without observed auroral lines could lead to inaccurate ionic abundance estimates. While $\log(\text{N}/\text{O})$ measured from N^+/O^+ is relatively insensitive to temperature, the use of N IV with O III to obtain the ionic abundances at $z > 5$ can also suffer systematic biases from shock-heating effects.

5.3 Shock Compression

Rankine-Hugoniot jump conditions predict compression of an adiabatic gas by a factor of 4 at the shock front, with an isothermal gas compression approaching a compression factor of ∞ (e.g., [Osterbrock & Ferland 2006](#)). The rapid cooling processes which occur after the shock front (i.e., through the shock) cause the gas to compress by as much as 4 dex while the gas cools and enters the 10^4 K recombination wake. At high velocities where the gas heating is much higher ($T_s \propto v_s^2$), rapid cooling causes the total shock to behave more isothermally, which can increase the gas compression rate

by orders of magnitude (e.g., Sutherland & Dopita 2017). We find typical compression factors of 2 dex across all shock models with variations depending on magnetic field strength, shock velocity, and density (cf. Sutherland & Dopita 2017, §8, Figures 8-9). Magnetic fields can mitigate the compression effects of rapid cooling by exerting an outward magnetic pressure as the gas compresses, thereby reducing the radiative efficiency of the shock (e.g., Draine & McKee 1993); however, even for strong magnetic fields ($B \gtrsim 10\mu\text{G}$), we find that even low density gas (1 cm^{-3}) with $v_s = 100\text{ km s}^{-1}$ can readily achieve a 2 dex increase in density. Observations indicate that shock excitation is consistent with much higher electron densities (e.g., Ho et al. 2014). Given gas densities as high as $n_e \sim 10^5\text{ cm}^{-3}$ or more observed in some cases at $z > 5$ (e.g., Maiolino et al. 2024; Topping et al. 2024a), the post-shock densities of anywhere from $\sim 10^5$ to 10^8 cm^{-3} due to compression of $\sim 10^4\text{ cm}^{-3}$ gas are reasonable conditions to expect even at lower shock velocities of 100 km s^{-1} .

Among the forbidden and semi-forbidden transitions, the low 4P states of the N III] quintuplet are uniquely insensitive to collisional de-excitations and may experience a corresponding flux enhancement through collisional excitation. The comparably insensitive $^5\text{S}_2$ state of the O III] lines has a higher critical density with two readily excited states immediately below related to the optical [O III] doublet and auroral lines, making the O III] doublet less augmented by density than the N III] quintuplet. Thus, the reported nitrogen “excess” may be due in part to gas density enhancement via compression by shocks. The apparent suppression of C III] emission in nitrogen-loud galaxies is likewise consistent with shock compression given the substantially low critical density of the $^3\text{P}_2$ state. Properly accounting for these density effects may resolve the discrepancy between the C/N observed at $z \gtrsim 5$ with *JWST* and expectations from standard nucleosynthesis models (Arellano-Córdova et al. 2022; Topping et al. 2024a; Curti et al. 2024; Marques-Chaves et al. 2024, Arellano-Cordova et al. in prep a).

Dense gas conditions produced by shock compression, in particular lower velocity shocks, can provide the unique conditions for collisional suppression of C III] and excitation of the N III]. N IV serves primarily as an ionization diagnostic as it is only slightly less sensitive to density than C III]. Gas in the early Universe can be substantially more dense (e.g., Maiolino et al. 2024; Topping et al. 2024b), which may be facilitated by shock compression of the gas. Both Mrk 996 and the Sunburst arc exhibit unusually high gas densities as well ($\gtrsim 10^6\text{ cm}^{-3}$ and $\gtrsim 10^5\text{ cm}^{-3}$, respectively, Thuan et al. 2008; James et al. 2009; Pascale et al. 2023), further indicating density enhancement that can be explained by shock compression.

5.4 Reducing the Nitrogen Excess

Radiative shocks can account for much of the observed strengths of UV nitrogen lines, reducing the reported excesses in nitrogen abundance to levels consistent with those observed in the local Universe. Such an adjustment would not eliminate the possibility of surplus nitrogen; however, the reduced excess removes the necessity of invoking more complex and/or fine-tuned scenarios to account for the measured abundances. High $\log(\text{N}/\text{O})$ is reported for the Sunburst arc only when including the N III] quintuplet and is otherwise “typical” (Pascale et al. 2023), which may indicate density-augmented N III] flux. We suggest that shock compression could increase the gas density sufficiently to enhance N III], which in turn leads to overestimates of $\log(\text{N}/\text{O})$ in this object. Indeed, Castellano et al. (2024) find that assuming high densities of $n_e \sim 10^5\text{ cm}^{-3}$ and higher temperatures of $T_e \sim 3 \times 10^4\text{ K}$, conditions predicted for post-shock gas

in many of our models, can reduce $\log(\text{N}/\text{O})$ by at least ~ 0.1 dex. In addition to high $\log(\text{N}/\text{O})$ values, Topping et al. (2024a) find high densities ($n_e \sim 10^5\text{ cm}^{-3}$), high temperatures ($T_e \sim 2.4 \times 10^4\text{ K}$), and exceptionally weak [O II] $\lambda\lambda 3726, 29$ lines, which could be explained by suppression of [O II] via collisional de-excitation of its upper ^2D states (see Table 3). However, we note that Castellano et al. (2024), Topping et al. (2024a,b), and others compare $\text{N}^{+2} + \text{N}^{+3}$ to O^{+2} to obtain $\log(\text{N}/\text{O})$ and do not include an ionization correction factor to account for missing ion species N^+ , O^+ , and O^{+3} . These corrections are necessary as indicated by the ionization potentials in Table 2 and would further lower the apparent nitrogen excess by fully accounting for the oxygen abundance. Moreover, an appropriately calibrated temperature scaling relation could improve measurements of ionic abundances, thereby increasing the measured $12 + \log(\text{O}/\text{H})$ and the expected $\log(\text{N}/\text{O})$ values (e.g., Dors et al. 2020, Flury et al. in prep)

To test the degree to which the nitrogen excess persists in these objects, we rerun a subset of shock models in the low-velocity, low metallicity regime with a 0.5 dex increase in N/O with respect to the Nicholls et al. (2017) trend. We find that we are able to reproduce the majority of the emission line fluxes of nitrogen-excess galaxies with this 0.5 increase, which is consistent with observations of stars and low-metallicity SFGs in the local Universe (e.g., van Zee & Haynes 2006; Guseva et al. 2011; Stephenson et al. 2023, Arellano-Cordova in prep.). A 0.5 dex increase in N/O can arise from rapid mixing of Wolf Rayet ejecta with the ISM following standard stellar nucleosynthesis abundance yields (e.g., Higgins et al. 2024), an effect observed in nearby starburst galaxies like NGC 5253 (e.g., Kobulnicky et al. 1997; López-Sánchez et al. 2007; Abril-Melgarejo et al. 2024) and ESO 338-IG04 (e.g., Bik et al. 2018). The nitrogen-enhanced knot of the Sunburst arc has a stellar populations within the 3-6 Myr age range associated with Wolf-Rayet stars (Rivera-Thorsen et al. 2017; Emil Rivera-Thorsen et al. 2024; Vanzella et al. 2020; Pascale et al. 2023) while Mrk 996 exhibits strong Wolf-Rayet features (Thuan et al. 1996, 2008; James et al. 2009; Telles et al. 2014), suggesting that Wolf-Rayet stars are simultaneously enriching the ISM and driving winds which trigger the radiative shocks. Local dwarf starburst galaxies like ESO 338-IG04 exhibit Wolf-Rayet stars causing simultaneous nitrogen enrichment and wind-driven shocks (Bik et al. 2018), which provides direct evidence for such scenarios in massive star clusters.

6 FUTURE CONSIDERATIONS FOR MODELS

6.1 Shocked Photoionized Gas

Previous studies of shock-SFG “composites” have simply co-added the fluxes to illustrate a fractional contribution of each component to the total $\text{H}\beta$ flux (e.g., Jaskot & Ravindranath 2016; Chisholm et al. 2024). While such an approach is physical when shocks and photoionized regions simply fall in the same spectroscopic aperture, the sensitivity of radiative shocks to the precursor conditions precludes such an approach when the gas is simultaneously illuminated by a photoionizing SED independent of the shock. In the context of the bright nitrogen lines, a scenario where, e.g., Wolf Rayet stars are photoionizing gas which is subsequently shocked by a stellar wind or an AGN is photoionizing gas which is subsequently shocked by a radiatively driven wind (e.g., Riffel et al. 2021), a shock + photoionization mixture must be treated simultaneously within a single model (e.g., Dors et al. 2021). Such an approach may explain the particularly high N III]/C III] ratios observed for AGN candidates GNz11 and GS 3073

and could account simultaneously for heating and ionization of the precursor by the AGN and gas heating, ionization, and compression by the shock. Future work should entail detailed treatment of these combined effects in order to reproduce the extreme $z > 5$ galaxies, particularly those with AGN signatures.

6.2 Dust

The dust content of galaxies at $z > 5$ is disputed. Signatures of dust-poor or even dust-free galaxies are present in the early Universe (e.g., Cullen et al. 2024; Saxena et al. 2024); however, evidence for dust in SFGs persists out to at least $z \sim 8$ —even as early as $z \sim 12$ or more—with relatively weak evolution with redshift (e.g., Ciesla et al. 2024; Saxena et al. 2024). While our primary shock models contain no dust, our additional dust-rich models suggest its effects may be important to consider for a variety of physical reasons.

Full destruction of the dust grains by the hot post-shock conditions may not be a reasonable assumption as anywhere from 10 to 70% grains can survive the shock (e.g., Borkowski & Dwek 1995; Jones et al. 1996; Dopita et al. 2016). In cases of low-velocity shocks, models indicate that the rate of grain destruction decreases due to the decline in thermal sputtering and shattering (e.g., McKee et al. 1987). Dust grains can dramatically impact shocks since they are coupled to gas via drag and to the magnetic field via charge and may also serve as an important source of radiative cooling (Draine & McKee 1993). Therefore, the incorporation of dust, including the various destruction mechanisms, into shock models should be addressed in greater detail.

6.3 Catastrophic Cooling

Two objects we have considered in this study exhibit evidence for catastrophic cooling in addition to possible shock excitation: the Sunburst arc (Pascale et al. 2023) and Mrk 71 (Oey et al. 2023; Smith et al. 2023). Catastrophic cooling can occur in shocks (e.g., Falle 1975, 1981; Smith 1989) and can be associated with phenomena such as supernova remnants (e.g., Falle 1975, 1981; Smith 1989; Silich et al. 2007) and winds (Smith 1989; Wang 1995; Silich et al. 2004, 2007; Gray et al. 2019). Catastrophic cooling is more likely to occur in dense gas environments due to over-pressurization (e.g., Silich et al. 2004), which may be facilitated by shocks and made more common in denser gas environments such as those in Green Pea galaxies (e.g., Jaskot et al. 2019) or those at high redshift (e.g., Jones et al. 2024; Maiolino et al. 2024; Topping et al. 2024b; Zavala et al. 2024a,b). Shocks could further contribute to catastrophic cooling via Vishniac instabilities wherein small perturbations cause fragmentation of the shock into dense cloudlets (Vishniac 1983). Therefore, the effects of catastrophic cooling may be important for interpreting observations of galaxies with shock-like line emission.

We have compared archival catastrophic cooling predictions from Danekkar et al. (2022) to our models and find that they are similarly capable reproducing the augmented N III] $\lambda\lambda 1747$ –54 quintuplet but do not predict similar suppression of the [C III] $\lambda 1907$ line. We note that catastrophic cooling libraries are, to date, quite novel and as a result might not span the same range in ionization parameter, ionizing source, or metallicity as our or other models. Indeed, the available models, while immensely useful, apply strictly to catastrophic cooling in galactic winds. Future work should include more detailed, robust, and extensive catastrophic cooling model line predictions in a wider range of scenarios. If catastrophic cooling in shocks can explain the observations of galaxies at $z > 5$, it may also indicate

positive feedback in SFGs by suppressing winds and forming dense clouds (e.g., Silich et al. 2007; Jaskot et al. 2017) and could even promote Lyman continuum escape (e.g., Jaskot et al. 2019; Flury et al. 2024).

7 CONCLUSION

To assess the origins of the putative nitrogen excess observed in galaxies at $z > 5$, we compute a series of new excitation models for SFGs, AGN, and shocks using MAPPINGS with empirical chemical abundance and dust depletion patterns and new atomic data shared across all models to mitigate any systematic differences. We define excitation regimes by exploring a wide range of ionizing SEDs from stellar populations and AGN as well as a variety of shock conditions.

We assemble flux ratio diagrams motivated by a combination of observational and physical constraints:

- detectability of emission lines
- resolvability of emission lines
- insensitivity to extinction
- sensitivity to SED shape
- sensitivity to gas density
- insensitivity to metallicity

We compare emission line flux ratios from spectra of nitrogen-excess galaxies observed by *JWST* with our excitation diagnostics. From our assessment, we conclude that galaxies exhibiting unusually bright N III] and/or N IV] have spectra consistent with low-velocity shocks and cannot be explained by other phenomena such as photoionization by AGN or stellar populations. These nitrogen-excess galaxies, along with several reference galaxies, consistently fall in diagnostic regions associated with shock ionization when considering C III]/He II, C IV/He II, C IV/C III], and O III]/He II.

Of the diagnostics considered here, the C III] / He II vs O III] / He II and N III] / C III] vs O III] / He II diagrams best distinguish between shock ionization and photoionization, predominantly owing to ionization and compression effects from the shock. To distinguish between different photoionization mechanisms, we recommend N IV] / C III] vs O III] / He II when O III] can be resolved from He II. If He II is not resolved from O III], the C III] / C IV] vs C IV] / (He II + O III]) can be used to distinguish SFGs from shocks and most AGN scenarios with the caveat that the C IV] doublet can suffer from stellar contamination.

We find an exceptional ability of N III] and N IV] to distinguish between shock and AGN excitation, defining a unique diagnostic space for shocks. Due to the relatively constant C/N with respect to $12 + \log(O/H)$ and metallicity in general, the N III]/C III] and N IV]/C III] diagnostic flux ratios provide an optimal means for distinguishing ionizing mechanisms. Both the nitrogen-excess galaxies and the reference galaxies consistent with shocks fall in the model-defined region for shocks, confirming the success of N III] and N IV] as shock diagnostics. To demonstrate the shock nature of these galaxies, we find kinematic evidence in the reference galaxies indicative of winds with velocities of 100 - 200 km s⁻¹. These velocities are consistent with the shock velocities of models which best describe the emission line flux ratios, corroborating our interpretation that shocks are a key ionizing mechanism in these objects.

The clear evidence for shock excitation suggests complications in the measurement of “direct method” nitrogen and oxygen abundances due to compression, heating, and ionization of gas by shocks. Moreover, the nitrogen abundances of these galaxies need not be extreme in order to agree with ionization models, with $\log(N/O)$ 0.2–0.3 dex higher than expected at the reported $12 + \log(O/H)$. In

even the most extreme cases, such as CEERS 3073 and GN-z11, the nitrogen enhancement may well be only 0.5 dex, still within the dispersion of local extragalactic observations (e.g., van Zee & Haynes 2006; Guseva et al. 2011; Berg et al. 2012, Arellano-Córdova et al. in prep.). We interpret the implied 0.3 excess in nitrogen, combined with low velocity shocks, as evidence for enrichment and excitation via winds from Wolf Rayet stars. Proper consideration of the shock ionization and its effects on the measured emission line fluxes can reconcile observations with conventional chemical evolution models and abundance patterns measured in the local Universe.

ACKNOWLEDGEMENTS

We thank the anonymous referee for their insightful comments.

SRF acknowledges support from NASA/FINESST 80NSSC23K1433. SRF thanks C Morisset and A Alarie for insight regarding the implementation of MAPPINGS V, M Mingozi for assistance with the CLASSY observations, and K Duncan for suggestions regarding optimal release of the models.

This research is based in part on observations made with the NASA/ESA Hubble Space Telescope obtained from the Space Telescope Science Institute, which is operated by the Association of Universities for Research in Astronomy, Inc., under NASA contract NAS 5–26555. These observations are associated with programs GO 15840, 16213, 16261.

This work is based in part on observations made with the NASA/ESA/CSA James Webb Space Telescope. The data were obtained from the Mikulski Archive for Space Telescopes at the Space Telescope Science Institute, which is operated by the Association of Universities for Research in Astronomy, Inc., under NASA contract NAS 5-03127 for JWST. These observations are associated with programs GTO 1180, 1181, 1210, 1286, GO 1895, 1963, 3215. The authors acknowledge the JADES and CEERS teams for developing their observing programs with a zero-exclusive-access period.

This publication made use of the MAPPINGS V software, which utilizes the CHIANTI database. CHIANTI is a collaborative project involving George Mason University, the University of Michigan (USA), University of Cambridge (UK) and NASA Goddard Space Flight Center (USA).

We acknowledge the use of the following software, repositories, and other digital resources: BPASS (Byrne et al. 2022), CHIANTI (Del Zanna et al. 2021), EOMS (Alarie & Morisset 2019), MAPPINGS V (Sutherland & Dopita 2017; Sutherland et al. 2018), matplotlib (Hunter 2007), numpy (van der Walt et al. 2011), oxaf (Thomas et al. 2016), scipy (P. Virtanen 2020), Starburst99 (Leitherer et al. 1999, 2014; Levesque et al. 2012), vygrboi (github.com/sflury/vygrboi)

For the purpose of open access, the author has applied a Creative Commons Attribution (CC BY) licence to any Author Accepted Manuscript version arising from this submission.

DATA AVAILABILITY

The predicted emission line fluxes, abundance patterns, gas conditions, and properties of key ions for the models presented here will be made available online at <http://dx.doi.org/10.5281/zenodo.14140949>. Ionizing SEDs not publicly attainable elsewhere will be made available on request.

REFERENCES

- Abril-Melgarejo V., James B. L., Aloisi A., Mingozi M., Lebouteiller V., Hernandez S., Kumari N., AAS Journals Data Editors 2024, *ApJ*, **973**, 173
- Alarie A., Morisset C., 2019, *Rev. Mex. Astron. Astrofis.*, **55**, 377
- Allen M. G., Groves B. A., Dopita M. A., Sutherland R. S., Kewley L. J., 2008, *ApJS*, **178**, 20
- Arellano-Córdova K. Z., Rodríguez M., 2020, *MNRAS*, **497**, 672
- Arellano-Córdova K. Z., et al., 2022, *ApJ*, **935**, 74
- Arroyo-Polonio A., et al., 2024, *A&A*, **687**, A77
- Backhaus B. E., et al., 2022, *ApJ*, **926**, 161
- Baldwin J. A., Phillips M. M., Terlevich R., 1981, *PASP*, **93**, 5
- Berg D. A., et al., 2012, *ApJ*, **754**, 98
- Berg D. A., et al., 2022, *ApJS*, **261**, 31
- Bik A., Östlin G., Menacho V., Adamo A., Hayes M., Herenz E. C., Melinder J., 2018, *A&A*, **619**, A131
- Binette L., Dopita M. A., Tuohy I. R., 1985, *ApJ*, **297**, 476
- Binette L., et al., 2024, *A&A*, **684**, A53
- Borkowski K. J., Dwek E., 1995, *ApJ*, **454**, 254
- Brinchmann J., Kunth D., Durret F., 2008, *A&A*, **485**, 657
- Bunker A. J., et al., 2023, *A&A*, **677**, A88
- Byrne C. M., Stanway E. R., Eldridge J. J., McSwiney L., Townsend O. T., 2022, *MNRAS*, **512**, 5329
- Castellano M., et al., 2024, *arXiv e-prints*, p. arXiv:2403.10238
- Chisholm J., Rigby J. R., Bayliss M., Berg D. A., Dahle H., Gladders M., Sharon K., 2019, *ApJ*, **882**, 182
- Chisholm J., et al., 2024, *MNRAS*, **534**, 2633
- Ciesla L., et al., 2024, *arXiv e-prints*, p. arXiv:2412.02557
- Cullen F., et al., 2024, *MNRAS*, **531**, 997
- Curti M., et al., 2024, *arXiv e-prints*, p. arXiv:2407.02575
- Danehar A., Oey M. S., Gray W. J., 2022, *ApJ*, **937**, 68
- Davies R. L., et al., 2016, *ApJ*, **824**, 50
- Del Zanna G., Dere K. P., Young P. R., Landi E., 2021, *ApJ*, **909**, 38
- Dopita M. A., 1995, *Ap&SS*, **233**, 215
- Dopita M. A., Sutherland R. S., 1996, *ApJS*, **102**, 161
- Dopita M. A., Groves B. A., Sutherland R. S., Binette L., Cecil G., 2002, *ApJ*, **572**, 753
- Dopita M. A., et al., 2005, *ApJ*, **619**, 755
- Dopita M. A., et al., 2006, *ApJ*, **647**, 244
- Dopita M. A., Sutherland R. S., Nicholls D. C., Kewley L. J., Vogt F. P. A., 2013, *ApJS*, **208**, 10
- Dopita M. A., et al., 2014, *A&A*, **566**, A41
- Dopita M. A., et al., 2015, *ApJ*, **801**, 42
- Dopita M. A., Seitzzahl I. R., Sutherland R. S., Vogt F. P. A., Winkler P. F., Blair W. P., 2016, *ApJ*, **826**, 150
- Dors O. L., Maiolino R., Cardaci M. V., Hägele G. F., Krabbe A. C., Pérez-Montero E., Armah M., 2020, *MNRAS*, **496**, 3209
- Dors O. L., Contini M., Riffel R. A., Pérez-Montero E., Krabbe A. C., Cardaci M. V., Hägele G. F., 2021, *MNRAS*, **501**, 1370
- Draine B. T., McKee C. F., 1993, *ARA&A*, **31**, 373
- Ekström S., et al., 2012, *A&A*, **537**, A146
- Emil Rivera-Thorsen T., et al., 2024, *A&A*, **690**, A269
- Esteban C., Peimbert M., Torres-Peimbert S., Rodríguez M., 2002, *ApJ*, **581**, 241
- Esteban C., Bresolin F., Peimbert M., García-Rojas J., Peimbert A., Mesa-Delgado A., 2009, *ApJ*, **700**, 654
- Falle S. A. E. G., 1975, *MNRAS*, **172**, 55
- Falle S. A. E. G., 1981, *MNRAS*, **195**, 1011
- Feltre A., Charlot S., Gutkin J., 2016, *MNRAS*, **456**, 3354
- Ferland G. J., et al., 2017, *Rev. Mex. Astron. Astrofis.*, **53**, 385
- Flury S. R., et al., 2024, *arXiv e-prints*, p. arXiv:2409.12118
- Georgy C., et al., 2013, *A&A*, **558**, A103
- Gray W. J., Oey M. S., Silich S., Scannapieco E., 2019, *ApJ*, **887**, 161
- Groves B. A., Dopita M. A., Sutherland R. S., 2004, *ApJS*, **153**, 9
- Guseva N. G., Izotov Y. I., Stasińska G., Fricke K. J., Henkel C., Papaderos P., 2011, *A&A*, **529**, A149
- Gutkin J., Charlot S., Bruzual G., 2016, *MNRAS*, **462**, 1757

- Heckman T. M., et al., 2011, *ApJ*, **730**, 5
- Heckman T. M., Alexandroff R. M., Borthakur S., Overzier R., Leitherer C., 2015, *ApJ*, **809**, 147
- Henry R. B. C., Edmunds M. G., Köppen J., 2000, *ApJ*, **541**, 660
- Higgins E. R., Vink J. S., Hirschi R., Laird A. M., Sander A. A. C., 2024, *MNRAS*, **533**, 1095
- Hillier D. J., Miller D. L., 1998, *ApJ*, **496**, 407
- Hillier D. J., Miller D. L., 1999, *ApJ*, **519**, 354
- Ho I. T., et al., 2014, *MNRAS*, **444**, 3894
- Hunter J. D., 2007, *Computing in Science Engineering*, **9**, 90
- Isobe Y., et al., 2023, *ApJ*, **959**, 100
- Izotov Y. I., Foltz C. B., Green R. F., Guseva N. G., Thuan T. X., 1997, *ApJ*, **487**, L37
- Izotov Y. I., Schaerer D., Blecha A., Royer F., Guseva N. G., North P., 2006, *A&A*, **459**, 71
- Izotov Y. I., Thuan T. X., Guseva N. G., 2021, *MNRAS*, **508**, 2556
- James B. L., Tsamis Y. G., Barlow M. J., Westmoquette M. S., Walsh J. R., Cuisinier F., Exter K. M., 2009, *MNRAS*, **398**, 2
- Jaskot A. E., Ravindranath S., 2016, *ApJ*, **833**, 136
- Jaskot A. E., Oey M. S., Scarlata C., Dowd T., 2017, *ApJ*, **851**, L9
- Jaskot A. E., Dowd T., Oey M. S., Scarlata C., McKinney J., 2019, *ApJ*, **885**, 96
- Jenkins E. B., 2009, *ApJ*, **700**, 1299
- Jenkins E. B., 2014, *arXiv e-prints*, p. arXiv:1402.4765
- Ji X., et al., 2024, *arXiv e-prints*, p. arXiv:2404.04148
- Jin C., Ward M., Done C., Gelbord J., 2012, *MNRAS*, **420**, 1825
- Jones A. P., Tielens A. G. G. M., Hollenbach D. J., 1996, *ApJ*, **469**, 740
- Jones G. C., et al., 2024, *arXiv e-prints*, p. arXiv:2405.12955
- Jung I., Ravindranath S., Jaskot A. E., Ferguson H. C., James B. L., 2024, *arXiv e-prints*, p. arXiv:2409.11460
- Kewley L. J., Nicholls D. C., Sutherland R., Rigby J. R., Acharya A., Dopita M. A., Bayliss M. B., 2019, *ApJ*, **880**, 16
- Kobayashi C., Ferrara A., 2024, *ApJ*, **962**, L6
- Kobayashi C., Karakas A. I., Lugaro M., 2020, *ApJ*, **900**, 179
- Kobulnicky H. A., Skillman E. D., Roy J.-R., Walsh J. R., Rosa M. R., 1997, *ApJ*, **477**, 679
- Kramida A., Yu. Ralchenko Reader J., and NIST ASD Team 2023, NIST Atomic Spectra Database (ver. 5.11), [Online]. Available: <https://physics.nist.gov/asd> [2024, October 21]. National Institute of Standards and Technology, Gaithersburg, MD.
- Kroupa P., 2001, *MNRAS*, **322**, 231
- Larson R. L., et al., 2023, *ApJ*, **953**, L29
- Leitherer C., et al., 1999, *ApJS*, **123**, 3
- Leitherer C., Ekström S., Meynet G., Schaerer D., Agienko K. B., Levesque E. M., 2014, *ApJS*, **212**, 14
- Levesque E. M., Richardson M. L. A., 2014, *ApJ*, **780**, 100
- Levesque E. M., Leitherer C., Ekstrom S., Meynet G., Schaerer D., 2012, *ApJ*, **751**, 67
- López-Sánchez Á. R., Esteban C., García-Rojas J., Peimbert M., Rodríguez M., 2007, *ApJ*, **656**, 168
- Luridiana V., Morisset C., Shaw R. A., 2015, *A&A*, **573**, A42
- Mainali R., et al., 2022, *ApJ*, **940**, 160
- Maiolino R., et al., 2024, *Nature*, **627**, 59
- Marques-Chaves R., et al., 2024, *A&A*, **681**, A30
- McKee C. F., Hollenbach D. J., Seab G. C., Tielens A. G. G. M., 1987, *ApJ*, **318**, 674
- Medling A. M., et al., 2015, *MNRAS*, **448**, 2301
- Mingozzi M., et al., 2022, *ApJ*, **939**, 110
- Mingozzi M., et al., 2024, *ApJ*, **962**, 95
- Nandal D., Regan J. A., Woods T. E., Farrell E., Ekström S., Meynet G., 2024a, *A&A*, **683**, A156
- Nandal D., Sibony Y., Tsiatsiou S., 2024b, *A&A*, **688**, A142
- Nicholls D. C., Sutherland R. S., Dopita M. A., Kewley L. J., Groves B. A., 2017, *MNRAS*, **466**, 4403
- Oey M. S., Herrera C. N., Silich S., Reiter M., James B. L., Jaskot A. E., Micheva G., 2017, *ApJ*, **849**, L1
- Oey M. S., et al., 2023, *ApJ*, **958**, L10
- Osterbrock D., Ferland G., 2006, *Astrophysics of Gaseous Nebulae and Active Galactic Nuclei*. University Science Books
- P. Virtanen R. Gommers T. O., 2020, *Nature Methods*, **17**, 261–272
- Pascale M., Dai L., McKee C. F., Tsang B. T. H., 2023, *ApJ*, **957**, 77
- Pauldrach A. W. A., Lennon M., Hoffmann T. L., Sellmaier F., Kudritzki R. P., Puls J., 1998, in Howarth I., ed., *Astronomical Society of the Pacific Conference Series Vol. 131, Properties of Hot Luminous Stars*. p. 258
- Petrosian A. R., Boulesteix J., Comte G., Kunth D., Lecoarer E., 1997, *A&A*, **318**, 390
- Phillips J. P., 2008, *New Astron.*, **13**, 60
- Rich J. A., Kewley L. J., Dopita M. A., 2011, *ApJ*, **734**, 87
- Rich J. A., Kewley L. J., Dopita M. A., 2015, *ApJS*, **221**, 28
- Riffel R. A., et al., 2021, *MNRAS*, **501**, L54
- Rivera-Thorsen T. E., et al., 2017, *A&A*, **608**, L4
- Rogers N. S. J., Skillman E. D., Pogge R. W., Berg D. A., Moustakas J., Croxall K. V., Sun J., 2021, *ApJ*, **915**, 21
- Saxena A., et al., 2024, *arXiv e-prints*, p. arXiv:2411.14532
- Schaerer D., Marques-Chaves R., Xiao M., Korber D., 2024, *A&A*, **687**, L11
- Senchyna P., Plat A., Stark D. P., Rudie G. C., 2023, *arXiv e-prints*, p. arXiv:2303.04179
- Shirazi M., Brinchmann J., 2012, *MNRAS*, **421**, 1043
- Shull J. M., McKee C. F., 1979, *ApJ*, **227**, 131
- Silich S., Tenorio-Tagle G., Rodríguez-González A., 2004, *ApJ*, **610**, 226
- Silich S., Tenorio-Tagle G., Muñoz-Tuñón C., 2007, *ApJ*, **669**, 952
- Smith M. D., 1989, *MNRAS*, **238**, 235
- Smith L. J., et al., 2023, *ApJ*, **958**, 194
- Steidel C. C., Erb D. K., Shapley A. E., Pettini M., Reddy N., Bogosavljević M., Rudie G. C., Rakic O., 2010, *ApJ*, **717**, 289
- Stephenson M. G., Arellano-Córdova K. Z., Berg D. A., Mingozzi M., James B. L., 2023, *Research Notes of the American Astronomical Society*, **7**, 31
- Stevens M. L., Shull J. M., Danforth C. W., Tilton E. M., 2014, *ApJ*, **794**, 75
- Sutherland R. S., Dopita M. A., 2017, *ApJS*, **229**, 34
- Sutherland R. S., Bicknell G. V., Dopita M. A., 1993, *ApJ*, **414**, 510
- Sutherland R., Dopita M., Binette L., Groves B., 2018, MAPPINGS V: Astrophysical plasma modeling code, Astrophysics Source Code Library, record ascl:1807.005
- Telles E., Thuan T. X., Izotov Y. I., Carrasco E. R., 2014, *A&A*, **561**, A64
- Thomas A. D., Groves B. A., Sutherland R. S., Dopita M. A., Kewley L. J., Jin C., 2016, *ApJ*, **833**, 266
- Thuan T. X., Izotov Y. I., Lipovetsky V. A., 1996, *ApJ*, **463**, 120
- Thuan T. X., Izotov Y. I., Lipovetsky V. A., 1997, *ApJ*, **477**, 661
- Thuan T. X., Hunt L. K., Izotov Y. I., 2008, *ApJ*, **689**, 897
- Topping M. W., et al., 2024a, *arXiv e-prints*, p. arXiv:2407.19009
- Topping M. W., et al., 2024b, *MNRAS*, **529**, 3301
- Vanzella E., et al., 2020, *MNRAS*, **499**, L67
- Veilleux S., Osterbrock D. E., 1987, *ApJS*, **63**, 295
- Verner D. A., Ferland G. J., Korista K. T., Yakovlev D. G., 1996, *ApJ*, **465**, 487
- Villar-Martin M., Tadhunter C., Clark N., 1997, *A&A*, **323**, 21
- Vink J. S., 2023, *A&A*, **679**, L9
- Vishniac E. T., 1983, *ApJ*, **274**, 152
- Wang B., 1995, *ApJ*, **444**, 590
- Welch B., et al., 2024, *arXiv e-prints*, p. arXiv:2405.06631
- Xu Y., et al., 2022, *ApJ*, **929**, 134
- Zavala J. A., et al., 2024a, *Nature Astronomy*,
- Zavala J. A., et al., 2024b, *arXiv e-prints*, p. arXiv:2411.03593
- Zhu P., Kewley L. J., Sutherland R. S., 2023, *ApJ*, **954**, 175
- van Zee L., Haynes M. P., 2006, *ApJ*, **636**, 214
- van der Walt S., Colbert S. C., Varoquaux G., 2011, *Computing in Science Engineering*, **13**, 22

This paper has been typeset from a \LaTeX file prepared by the author.